International Journal of Mechanical System Dynamics

WILEY

IJMSD International Journal of Mechanical System Dynamics Open Access

RESEARCH ARTICLE OPEN ACCESS

Uncertainty Quantification for Nonlinear Vibration of Supercritical Drive Shaft With a Dry Friction Damper

Liyao Song[1] | Meijun Liao[1,2] | Weifang Chen[1] | Rupeng Zhu[1] | Dan Wang[1]

[1]National Key Laboratory of Science and Technology on Helicopter Transmission, Nanjing University of Aeronautics and Astronautics, Nanjing, People's Republic of China | [2]National Key Laboratory of Science and Technology on Helicopter Transmission, AECC Hunan Aviation Powerplant Research Institute, Zhuzhou, People's Republic of China

Correspondence: Dan Wang (wangdan_053@nuaa.edu.cn)

Received: 2 January 2025 | **Revised:** 6 March 2025 | **Accepted:** 26 March 2025

Funding: This study was funded by the Postgraduate Research & Practice Innovation Program of Jiangsu Province (Grant No. KYCX24_0552) and National Natural Science Foundation of China (Grant No. 52005253).

Keywords: modal superposition | rub-impact | sparse grid | supercritical shaft | uncertainty quantification

ABSTRACT

The supercritical drive shaft is becoming increasingly popular in helicopter transmission system. Dry friction dampers are specially employed to ensure the supercritical shafts crossing the critical speed safely. Due to design tolerances, manufacturing errors and time-varying factors, the parameters of the damper are inherently uncertain, affecting the safety performance of the rotor system. This paper incorporates these parameter uncertainties to investigate the dynamic response uncertainties of a supercritical shaft and dry friction damper system, which is characterized by its high dimensionality and nonlinear behaviors of rub-impact and dry friction. The nonintrusive Polynomial Chaos Expansion (PCE) is adopted to achieve the propagation of uncertainties in the rotorsystem. To achieve efficient uncertainty quantification for this high-dimensional nonlinear system, a double-layer dimensionality reduction algorithm combining modal superposition with sparse grid technique has been applied. In the computational workflow, the inner layer uses modal superposition and the outer layer uses sparse grid techniques. The stochastic dynamic response of the rotorsystem is analyzed considering the uncertainty of five design parameters of the damper. Furthermore, as a post-processing of the PCE coefficients, the Sobol global sensitivity analysis is conveniently conducted. The influence of individual parameters or groups of parameters on the dynamic response is studied. A multi-objective optimization design for the key parameters is then carried out based on the established PCE model. The dynamic model and optimization design method are verified by experiments. The results will benefit uncertainty quantification analysis of high-dimensional nonlinear rotorsystem.

1 | Introduction

The supercritical transmission system, with its advantages of high operating speed, small torque transmission, and fewer supports, can better meet the development needs of aircraft transmission systems for high efficiency, reliability, and safety. A typical example is the supercritical tail rotor drive shaft system of helicopters [1, 2]. However, due to their large span and high flexibility, supercritical transmission shafts experience significant lateral vibration issues, which may result in bending or even failure. To ensure the supercritical shafts crossing the critical speed safely, dry friction dampers are specially designed for mitigating the lateral vibrations, as shown in Figure 1.

The performance of dry friction dampers is crucial in determining whether the rotor can safely traverse its critical speed. Therefore, understanding the dynamics of these dampers and optimizing their design is essential for the safe operation of

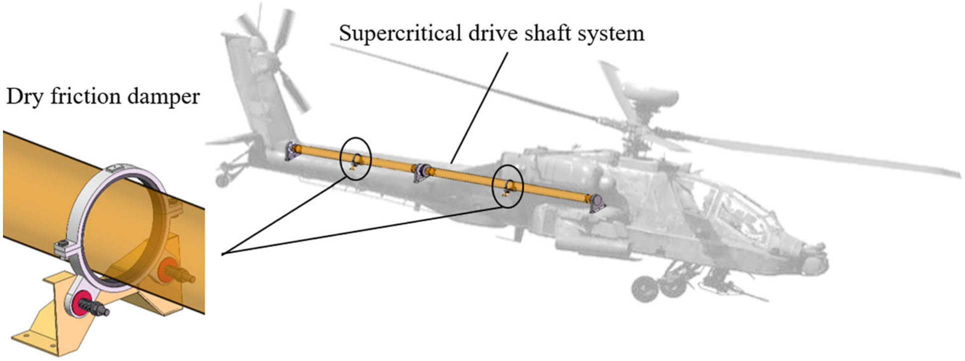

FIGURE 1 | Supercritical tail drive shaft system of a helicopter.

supercritical rotors. There exists rub-impact coupling with stick-slip dry friction forces in the supercritical rotor system with dry friction damper causing strong nonlinearity and complex dynamic behaviors. A series of research achievements have been made on the nonlinear vibration of the supercritical rotor system with dry friction damper. Dżygadło and Perkowski [3–5] first verified the effectiveness of the dry friction damper in damping transcritical vibrations of a helicopter supercritical drive shaft. Based on a macroslip friction model, Özaydın et al. [6, 7] established three low-dimensional dynamical models: a one-dimensional model without clearance, a one-dimensional model with clearance, and a two-dimensional model without clearance. Huang et al. [8] mainly focus on the coupling effect between misalignment and rub-impact, and further studied the effects of viscous internal damping and gyroscopic moment on stability and phase difference of a supercritical drive shaft [9]. Wang et al. [10, 11] built a two-dimensional Jeffcott rotor model to conveniently apply the harmonic balance method and Floquet theory to analyze the stability of the supercritical drive shaft. Zhu et al. [12] studied the self-excited vibration and rub-impact occurring in a supercritical helicopter tail transmission system equipped with floating spline and dry friction damper. In previous studies, the parameters of dry friction dampers are treated as deterministic variables, with a focus on analyzing their impact on dynamic response, lacking parameter design methodologies. However, the parameters are actually often subjected to many potential uncertainties that may rise from design tolerances, manufacturing errors and time-varying factors, such as installation clearance errors, wear between contact interfaces, and so on. These uncertainties will inevitably cause the rotor system response indeterministic, affecting the reliability design. It is crucial to acknowledge and address these uncertainties to ensure the optimal performance and reliability of rotor system. Therefore, an anticipated improvement of previous studies is to incorporate the uncertainties of the parameters for prediction of the rotorsystem response, and to further perform sensitivity analysis and optimization design on the key parameters of the damper.

The uncertainty quantification (UQ) of rotordynamics has attracted increasing attention, and several stochastic methods to rotordynamics have been applied, including classic Monte Carlo Simulations (MCS), perturbation method, Advanced Kriging model and the Polynomial Chaos Expansion (PCE), and both random and interval uncertainties of parameters has been in consideration in the past research [13]. By building statistics from responses obtained by sampling uncertain inputs through a large number of runs, MCS is the most robust but computationally expensive tools. To avoid this, the perturbation method is proposed based on the expansion of random quantities into Taylor series and the Neumann method based on Neumann series expansion [14–16]. But the perturbation method provides acceptable results only for small random fluctuations, and it is an intrusive method not applicable for large freedom and complexity rotor system. Kriging model is also popularly applied to UQ of rotordynamics. Denimal and Sinou [17] proposed a hybrid surrogate-model for UQ and global sensitivity analysis (GSA) of rotordynamics, which combines Kriging and PCE. Ma et al. [18] adopted an advanced Kriging model for propagation of uncertainties in fixed-point rub-impact rotor system. The PCE, which can work in a nonintrusive way, is an efficient uncertainty propagation method by expanding the response onto a particular basis of the probability space [19, 20]. Specifically, by combining harmonic balance method and PCE, Didier et al. proposed a stochastic harmonic balance method [21] and applied it to nonlinear rotor systems with unbalance, misalignment and initial bending to obtain the uncertain nonlinear response [22]. After that, they further proposed multidimensional stochastic harmonic balance method [23] and studied on the stochastic response of rotor with non-regular nonlinearities [24] and local non-linearities [25]. Fu et al. proposed the PCE in combination with the Chebyshev Surrogate Method (CSM) [26] on the uncertainty quantification of rotor systems with both random uncertain parameters and interval uncertain parameters, and the Chebyshev Convex Method [27] on interval uncertain quantification. They further studied the stochastic response of the uncertain notched rotor systems [28] and dual-rotor systems [29, 30]. Zhang et al. [31] analyzed the nonlinear stochastic dynamics of a fixed-point rub-impact rotor system based on harmonic balance method combined with PCE, in which the rotor is simplified as a Jeffcott rotor model. Ma et al. [32] adopted PCE to the UQ and GSA of the self-excited vibration which occurs in the spline-shafting system.

With the advantage of substantial mathematical foundation and excellent performance in uncertainty propagation, PCE is widely applied in UQ of rotor system. In this paper, the PCE method is employed to contribute a stochastic model for the uncertain supercritical rotor and dry friction damper system. While the classic Jeffcott model is straightforward to analyze, its two-degree-of-freedom structure limits the representation of the rotor system's dynamic characteristics. In contrast, finite element models provide richer dynamic information but significantly increase the system's degrees of freedom, requiring substantial computational resources for UQ. In addition, when employing PCE methods for uncertainty quantification, there exists so-called "curse of dimensionality." To address the challenges of high dimensionality, this paper employs a double-layer dimensionality reduction algorithm combining modal superposition with sparse grid technique. This approach is applied to effectively assess the vibration damping performance of the damper. After that a GSA is conveniently performed by computing the Sobol indices analytically as a post-processing of the PCE coefficients [33].

The rest of the paper is organized as follows. Section 2 describes the dynamic modeling of a supercritical drive shaft with a dry friction damper under uncertainty. Section 3 provides a detailed explanation of the double-layer dimensionality reduction algorithm. Section 4 presents a comprehensive uncertainty propagation analysis along with comparative discussions of various parameter cases. The results are compared with those obtained from MCS to demonstrate the validity and efficiency of the established model. Then a multi-objective optimization design to enhance the vibration damping performance of dry friction damper is carried out. A transcritical vibration experiment of a supercritical rotor with dry friction damper is conducted to verify the effectiveness of dynamic model and optimization method. Finally, the conclusions of the present work are summarized in Section 5.

2 | Dynamic Model of the Rotor System Under Uncertain Parameters

2.1 | Dynamic Model of the Rotor System

In this study, a typical single-span supercritical transmission system with a dry friction damper is considered, as shown in Figure 2. It consists of a hollow rotating shaft, two isotropic elastic supports and a dry friction damper installed in the middle of the shaft span to ensure that the shaft pass through the first critical speed safely. The damper is mainly composed of a movable rub-impact ring made in half-half type for easy disassembling and assembling, two pre-tightening springs, four friction discs, two bolts, and a base, as illustrated in Figure 2C. There exist clearances δ_1, δ_2 between the rub-impact ring and the shaft, as well as the ring and the bolts. There exists friction on the surfaces between the friction discs and the rub-impact ring, and the friction force can be set by varying the pre-tightening spring force.

In Figure 3A, an inertial coordinate system ($Oxyz$) is associated with the centroid of the support, and the cross-section of the shaft is assumed to remain in the yz plane. The supports at both end of the shaft are modeled ideally by isotropic linear springs with stiffness k_0. The shaft is modeled by the finite element method with Timoshenko beam theory, divided into N elements, $N+1$ nodes. Each node has 4 degrees of freedom, including translation along the y, z directions and rotation around the y, z directions. Considering that the rotor in the system is a slender flexible shaft without a disk, the influence of the gyroscopic effect is minimal, as detailed in the appendix. To facilitate the application of the modal superposition method, the gyroscopic effect is ignored accordingly.

The damper is located at the middle node of the shaft, and the rotation of the rub-impact ring, which has a mass m_r, is neglected. The nonlinear forces of the damper include rub-impact forces between the shaft and the rub-impact ring, as well as the ring and the bolts, and the dry friction force between rub-impact ring and friction discs. The rub-impact forces which are denoted as $\boldsymbol{f}_1$ and $\boldsymbol{f}_2$, include normal contact forces and tangential friction forces as shown in Figure 3B. The normal and tangential rub-impact force can be expressed as

$$f_{iN} = H(\varepsilon_i) k_i \varepsilon_i, \tag{1}$$

$$f_{iT} = H(\varepsilon_i) \mu_i f_{iN} \operatorname{sign}(v_i), \tag{2}$$

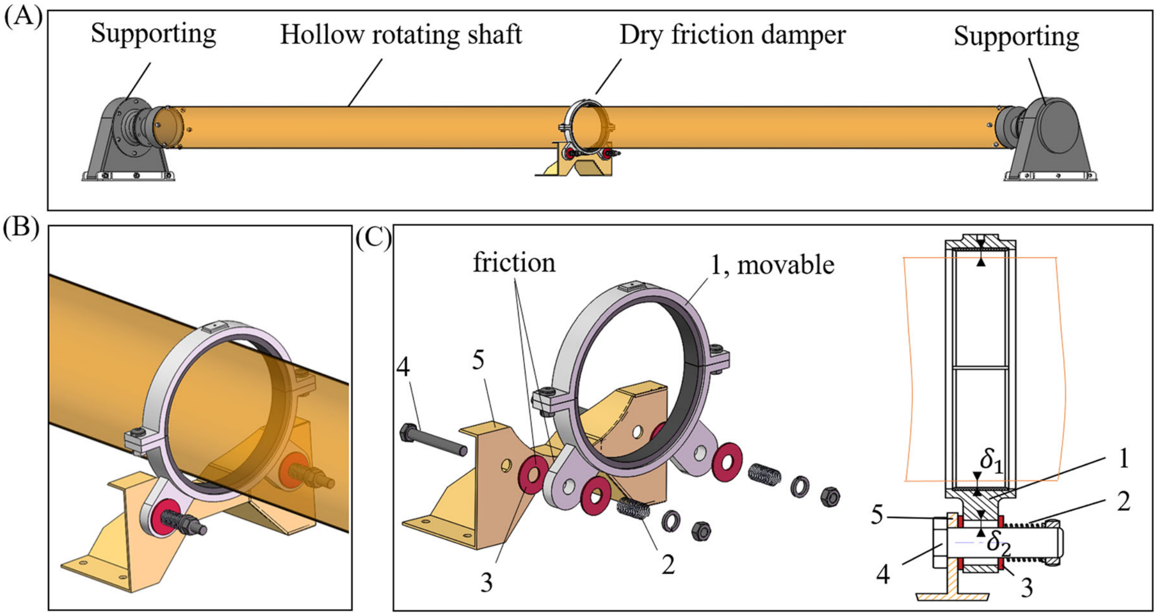

FIGURE 2 | A typical single-span supercritical transmission system with a dry friction damper. (A) 3-D model, (B) detailed view of dry friction damper; (C) detailed structures of the dry friction damper: 1—Half-half type rub-impact ring, 2—Pre-tightening spring, 3—Friction disc, 4—Bolt, 5—Base.

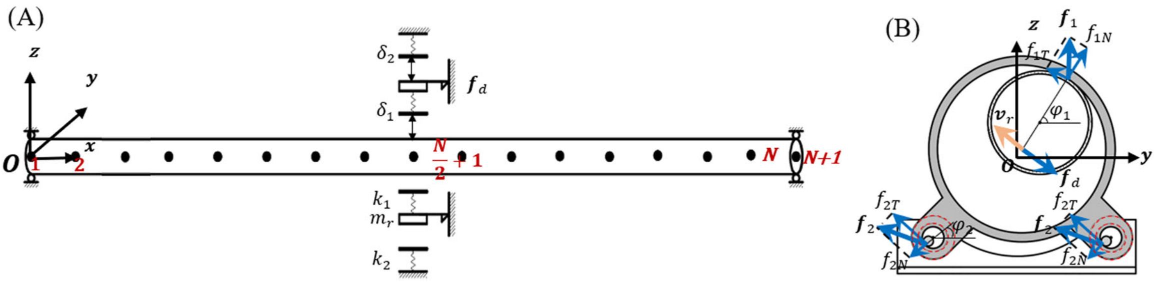

FIGURE 3 | Dynamic modeling of the system: (A) finite element model of a single-span supercritical shaft with dry friction damper and (B) schematic diagram of the rub-impact forces and dry friction force.

where $i = 1, 2$, represents the rub-impact between shaft and ring, ring and bolts respectively, $H(\varepsilon_i)$ is Heaviside function with $H(\varepsilon_i) = 1$ for $\varepsilon_i > 0$, and ε_i is the relative radial displacement at the contact point, k_1, k_2 are the contact stiffness, μ_1, μ_2 are the tangential friction coefficient at the interface, v_1, v_2 are the relative tangential velocity at the contact points. And their detailed expressions are provided in the appendix. The dry friction force $\boldsymbol{f}_d$ which opposites to velocity of the ring $\boldsymbol{v}_r$, as shown in Figure 3B, can be derived by

$$[f_{dy}, f_{dz}]^{\mathrm{T}} = -H(v_r) f_c \left[\frac{\dot{y}_r}{v_r}, \frac{\dot{z}_r}{v_r}\right]^{\mathrm{T}}, \tag{3}$$

where $H(v_r) = 1$ for $v_r > 0$, v_r is the absolute value of the velocity of the ring, with the detailed expression provided in the appendix. f_s is the pre-tightening force from springs and μ_3 is the sliding friction coefficient. f_c is the critical dry friction force, representing the product of f_s and μ_3, which determines the transition for the motion of the ring from stick to slip. The unbalance excitation on the shaft can be expressed as

$$[f_{ey}, f_{ez}]^{\mathrm{T}} = [me\dot{\phi}^2 \cos\phi + me\ddot{\phi}\sin\phi, me\dot{\phi}^2 \sin\phi - me\ddot{\phi}\cos\phi]^{\mathrm{T}}, \tag{4}$$

where m is the equivalent mass of the shaft and e is the eccentric distance, ϕ is the rotation angular of the shaft. Therefore, the equations of motion of the rotorsystem can be expressed as

$$\begin{bmatrix} \boldsymbol{m}_s & \\ & \boldsymbol{m}_r \end{bmatrix} \begin{bmatrix} \ddot{\boldsymbol{q}}_s \\ \ddot{\boldsymbol{q}}_r \end{bmatrix} + \begin{bmatrix} \boldsymbol{k}_s & \\ & \boldsymbol{k}_r \end{bmatrix} \begin{bmatrix} \boldsymbol{q}_s \\ \boldsymbol{q}_r \end{bmatrix} + \begin{bmatrix} \boldsymbol{c}_s & \\ & \boldsymbol{c}_r \end{bmatrix} \begin{bmatrix} \dot{\boldsymbol{q}}_s \\ \dot{\boldsymbol{q}}_r \end{bmatrix} = \begin{bmatrix} \boldsymbol{f}_s \\ \boldsymbol{f}_r \end{bmatrix}, \tag{5}$$

where $\boldsymbol{m}_s$, $\boldsymbol{k}_s$ and $\boldsymbol{c}_s$ are the mass, stiffness and damping matrices of the shaft, respectively, assembled with the support element. The stiffness matrix of the support node is $\mathrm{diag}(k_0, k_0, 0, 0)$. The damping matrix is calculated using Rayleigh damping, with its detailed expressions provided in the appendix. $\boldsymbol{m}_r$, $\boldsymbol{k}_r$ and $\boldsymbol{c}_r$ is the mass, stiffness and damping matrices of the ring, and the dynamic model of the ring is established by lumped mass method with $\boldsymbol{m}_r = \mathrm{diag}(m_r, m_r)$, $\boldsymbol{k}_r$ and $\boldsymbol{c}_r$ being ignored. $\boldsymbol{q}_s$, $\boldsymbol{q}_r$ are the displacement vectors of the shaft and ring, respectively. $\boldsymbol{f}_s$, $\boldsymbol{f}_r$ are the forces on shaft and ring, expressed as

$$\boldsymbol{f}_s = [0, 0, 0, 0 \cdots, f_{ey} - f_{1y}, f_{ez} - f_{1z}, 0, 0, \cdots 0, 0, 0, 0]^{\mathrm{T}}, \tag{6}$$

$$\boldsymbol{f}_r = [f_{1y} + 2f_{2y} + f_{dy}, f_{1z} + 2f_{2z} + f_{dz}]^{\mathrm{T}}, \tag{7}$$

where f_{1y}, f_{1z} and f_{2y}, f_{2z} are the components in y and z directions of $\boldsymbol{f}_1$ and $\boldsymbol{f}_2$, respectively. The drive shaft is divided into 16 elements and has 64 degrees of freedom. Including the two degrees of freedom from the damper, the system has a total of 66 degrees of freedom, which greatly increases the computational complexity compared to the Jeffcott rotor model.

2.2 | Uncertainty Propagation Based on PCE

The PCE method is applied to derive the uncertain dynamic response. In this system, five parameters of the damper are modeled as random variables, including the mass of the ring m_r, normal rub-impact stiffness k_1, tangential rub-impact friction coefficients μ_1, clearance δ_1 and critical dry friction force f_c. These parameters are denoted by vector $\boldsymbol{r}$, for example, $\boldsymbol{r} = [m_r, k_1, \mu_1, \delta_1, f_c]^{\mathrm{T}}$. All the uncertain parameters are considered to be independent. These uncertain parameters can be converted to standard random variables denoted as $\boldsymbol{\xi} = [\xi_1, \xi_2, \cdots, \xi_d]^{\mathrm{T}}$. d is the dimension of random variables and $d = 5$ in this model. According to the PCE method, the stochastic response can be written as a function of standard random variables, then the uncertain dynamic model of the rotorsystem can be written as

$$\begin{bmatrix} \boldsymbol{m}_s & \\ & \boldsymbol{m}_r \end{bmatrix} \begin{bmatrix} \ddot{\boldsymbol{q}}_s(\boldsymbol{\xi}) \\ \ddot{\boldsymbol{q}}_r(\boldsymbol{\xi}) \end{bmatrix} + \begin{bmatrix} \boldsymbol{k}_s & \\ & \boldsymbol{k}_r \end{bmatrix} \begin{bmatrix} \boldsymbol{q}_s(\boldsymbol{\xi}) \\ \boldsymbol{q}_r(\boldsymbol{\xi}) \end{bmatrix} + \begin{bmatrix} \boldsymbol{c}_s & \\ & \boldsymbol{c}_r \end{bmatrix} \begin{bmatrix} \dot{\boldsymbol{q}}_s(\boldsymbol{\xi}) \\ \dot{\boldsymbol{q}}_r(\boldsymbol{\xi}) \end{bmatrix} = \begin{bmatrix} \boldsymbol{f}_s(\boldsymbol{\xi}) \\ \boldsymbol{f}_r(\boldsymbol{\xi}) \end{bmatrix}. \tag{8}$$

$q(\boldsymbol{\xi})$ can be written as

$$\begin{aligned} q(\boldsymbol{\xi}) = b_0 \Psi_0 + \sum_{i_1=1}^{\infty} b_{i_1} \Psi_1(\xi_{i_1}) + \sum_{i_1=1}^{\infty} \sum_{i_2=1}^{i_1} b_{i_1 i_2} \Psi_2(\xi_{i_1}, \xi_{i_2}) \\ + \sum_{i_1=1}^{\infty} \sum_{i_2=1}^{i_1} \sum_{i_3=1}^{i_2} b_{i_1 i_2 i_3} \Psi_3(\xi_{i_1}, \xi_{i_2}, \xi_{i_3}) + \cdots, \end{aligned} \tag{9}$$

where $b_0, b_{i_1}, \cdots, b_{i_1 i_2 \cdots i_n}$ are the unknown expansion coefficient and $\Psi_n(\xi_{i_1}, \xi_{i_2}, \cdots, \xi_{i_n})$ is the n-order multi-dimensional orthogonal polynomials related to the distribution of $\boldsymbol{\xi}$, for example, Hermite polynomials for Gaussian distribution, Legendre polynomials for uniform distribution, Laguerre polynomials for gamma distribution, Jacobi polynomials for beta distribution [34]. In practice, expansion shall be truncated for computational purposes. Considering all d-dimensional orthogonal polynomials of order not exceeding p, the response can be approximated as follows:

$$q \approx \sum_{i=0}^{P-1} b_i \Psi_i(\boldsymbol{\xi}). \tag{10}$$

P is the number of unknown coefficients in this summation, which can be derived by

$$P = \frac{(p+d)!}{p!d!}. \tag{11}$$

The PCE coefficients can be evaluated by Galerkin projection and regression method of which the former is more robust [19]. Based on Galerkin projection, the coefficients are evaluated by

$$b_i = \frac{E[q(\boldsymbol{r})\Psi_i(\boldsymbol{\xi})]}{E[\Psi_i(\boldsymbol{\xi})^2]}, \quad i = 0, 1, \cdots, P-1, \tag{12}$$

where $E[\blacksquare]$ is expectation operator. When the coefficients are obtained, the mean and variance of the output q also can be easily derived from PCE as follows:

$$\mu_{PC} = E[q] = b_0\Psi_0, \tag{13}$$

$$D_{PC} = V[q] = \sum_{i=1}^{P-1} b_i{}^2 E[\Psi_i(\boldsymbol{\xi})^2], \tag{14}$$

where $V[\blacksquare]$ is the variance operator.

Once the PCE of rotor system is constructed, the Sobol indices can be directly derived from the PCE coefficients and the parameters most sensitive to the transcritical response can be ranked. These indices, called PC-based Sobol indices and denoted by $S_{i_1\cdots i_s}$ can be straightforwardly given as

$$S_{i_1\cdots i_s} = \frac{\sum_{\alpha\in\Omega_{i_1,\dots,i_s}} b_\alpha{}^2 E[\Psi_\alpha{}^2]}{D_{PC}}, \tag{15}$$

where Φ_α respresents all polynomials related only to $r_{i_1}, \cdots, r_{i_s}$, $1 \le s \le d$. For more details, Refs. [33, 35]. can be referred to. The first-order sensitivity indices $\boldsymbol{S}_i$ give the effect of each parameter taken alone whereas the higher order indices account for possible interact effect of various parameters. The total sensitivity indices $\boldsymbol{S}_i^{\mathrm{T}}$ evaluating the total effect of an input parameter are defined as the sum of all partial sensitivity indices $S_{i_1\cdots i_s}$ involving parameter r_i.

The primary challenge is to derive the expectations of $q(\boldsymbol{r})\Psi_i(\boldsymbol{\xi})$ and $\Psi_i(\boldsymbol{\xi})^2$. One of the main approaches to approximate the expectation is full factorial numerical integration (FFNI) which operates over a configuration space composed of specific configuration points. The configuration space of d-dimensional random variables based on FFNI is derived by direct tensor-product [36] as follows:

$$\Omega_d^n = \Omega_1^{N_1} \otimes \Omega_1^{N_2} \otimes \cdots \Omega_1^{N_j} \otimes \cdots \otimes \Omega_1^{N_d}, \tag{16}$$

where $\Omega_1^{N_j}$ represents the configuration space composed of N_j points of the jth dimensional variable, and $N_1 = \cdots N_j \cdots = N_d = K$ corresponds to algebraic accuracy of order $2K-1$. It is obvious that the number of configuration points increases exponentially with the dimension number of random variables, causing large compute load. Therefore, considering sparsizing configuration points of FFNI, the sparse grid numerical integration (SGNI) method is proposed [37]. On this basis, the improved sparse grid method has been further proposed and applied in the UQ of nonlinear systems [38]. SGNI constructs the configuration points by utilizing special tensor-product operations, which will be discussed in detail below.

3 | Double-Layer Dimensionality Reduction Algorithm Combining Modal Superposition With Sparse Grid Technique

Considering that directly quantifying uncertainties in this high-dimensional system would require significant computational resources, a double-layer dimensionality reduction algorithm combining modal superposition with sparse grid technique is applied in UQ of this system. The execution logic for UQ of the supercritical rotor system with dry friction damper is illustrated in Figure 4.

3.1 | Dynamic Modeling Through Modal Superposition

In this process, the inner layer uses modal superposition to reduce the degrees of freedom of the uncertain system. To conduct it, the vibration equation of the shaft is rewritten in the following form

$$\begin{bmatrix} 0 & \boldsymbol{m}_s \\ \boldsymbol{m}_s & \boldsymbol{c}_s \end{bmatrix} \frac{\mathrm{d}}{\mathrm{d}t} \begin{bmatrix} \dot{\boldsymbol{q}}_s \\ \boldsymbol{q}_s \end{bmatrix} + \begin{bmatrix} -\boldsymbol{m}_s & 0 \\ 0 & \boldsymbol{k}_s \end{bmatrix} \begin{bmatrix} \dot{\boldsymbol{q}}_s \\ \boldsymbol{q}_s \end{bmatrix} = \boldsymbol{0}. \tag{17}$$

Define $\boldsymbol{h} = \begin{bmatrix} \dot{\boldsymbol{q}}_s \\ \boldsymbol{q}_s \end{bmatrix}$, $\dot{\boldsymbol{h}} = \frac{\mathrm{d}}{\mathrm{d}t}\begin{bmatrix} \dot{\boldsymbol{q}}_s \\ \boldsymbol{q}_s \end{bmatrix}$, $\boldsymbol{A}_h = \begin{bmatrix} 0 & \boldsymbol{m}_s \\ \boldsymbol{m}_s & \boldsymbol{c}_s \end{bmatrix}$, $\boldsymbol{B}_h = \begin{bmatrix} -\boldsymbol{m}_s & 0 \\ 0 & \boldsymbol{k}_s \end{bmatrix}$, Equation (17) can be written as

$$\boldsymbol{A}_h \dot{\boldsymbol{h}} + \boldsymbol{B}_h \boldsymbol{h} = \boldsymbol{0}. \tag{18}$$

Let $\boldsymbol{h} = \boldsymbol{h}_0 e^{st}$, Equation (18) can be written as

$$-\boldsymbol{B}_h \boldsymbol{h}_0 = s\boldsymbol{A}_h \boldsymbol{h}_0. \tag{19}$$

By solving the generalized eigenvalue problem in Equation (19), the eigenvalues and eigenvectors can be obtained, which correspond to the modal frequencies and mode shapes. The mode shape matrix is denoted as $\boldsymbol{\Phi}$. The response of the shaft can be transformed from physical space to modal space as $\boldsymbol{q}_s(\boldsymbol{\xi}) = \boldsymbol{\Phi}\boldsymbol{q}_{sP}(\boldsymbol{\xi})$, and $\boldsymbol{q}_{sP}(\boldsymbol{\xi})$ is the uncertain response in modal space. By substituting it to Equation (8), it is can be derived that

$$\boldsymbol{m}_s\boldsymbol{\Phi}\ddot{\boldsymbol{q}}_{sP}(\boldsymbol{\xi}) + \boldsymbol{k}_s\boldsymbol{\Phi}\boldsymbol{q}_{sP}(\boldsymbol{\xi}) + \boldsymbol{c}_s\boldsymbol{\Phi}\dot{\boldsymbol{q}}_{sP}(\boldsymbol{\xi}) = \boldsymbol{f}_s(\boldsymbol{\xi}). \tag{20}$$

Multiply by matrix $\boldsymbol{\Phi}^{\mathrm{T}}$, then the uncertain dynamic equation in modal space can be derived as

$$\boldsymbol{m}_{sP}\ddot{\boldsymbol{q}}_{sP}(\boldsymbol{\xi}) + \boldsymbol{k}_{sP}\boldsymbol{q}_{sP}(\boldsymbol{\xi}) + \boldsymbol{c}_{sP}\dot{\boldsymbol{q}}_{sP}(\boldsymbol{\xi}) = \boldsymbol{f}_{sP}(\boldsymbol{\xi}), \tag{21}$$

where $\boldsymbol{m}_{sP} = \Phi^{\mathrm{T}}\boldsymbol{m}_s\Phi$, $\boldsymbol{k}_{sP} = \Phi^{\mathrm{T}}\boldsymbol{k}_s\Phi$, $\boldsymbol{c}_{sP} = \Phi^{\mathrm{T}}\boldsymbol{c}_s\Phi$, $\boldsymbol{f}_{sP}(\boldsymbol{\xi}) = \boldsymbol{\Phi}^{\mathrm{T}}\boldsymbol{f}_s(\boldsymbol{\xi})$. There are 64 degrees of freedom in Equation (21) corresponding to 64 order modes. By truncating the first n order modes from Equation (21), the truncated dynamic equation of the shaft is obtained as follows:

$$\boldsymbol{m}_{sP}^{n}\ddot{\boldsymbol{q}}_{sP}^{n}(\boldsymbol{\xi}) + \boldsymbol{k}_{sP}^{n}\boldsymbol{q}_{sP}^{n}(\boldsymbol{\xi}) + \boldsymbol{c}_{sP}^{n}\dot{\boldsymbol{q}}_{sP}^{n}(\boldsymbol{\xi}) = \boldsymbol{f}_{sP}^{n}(\boldsymbol{\xi}), \tag{22}$$

where $\boldsymbol{q}_{sP}^{n}(\boldsymbol{\xi})$, $\boldsymbol{m}_{sP}^{n}$, $\boldsymbol{k}_{sP}^{n}$, $\boldsymbol{c}_{sP}^{n}$ represent the truncated modal response, mass matrix, stiffness matrix, and damping matrix, respectively. $\boldsymbol{f}_{sP}^{n}(\boldsymbol{\xi})$ denotes the truncated external forces. The dynamic equations of the damper do not need to be transformed into modal space. Therefore, the uncertain dynamic equations can be rewritten as

$$\begin{bmatrix} \boldsymbol{m}_{sP}^{n} & \\ & \boldsymbol{m}_r \end{bmatrix} \begin{bmatrix} \ddot{\boldsymbol{q}}_{sP}^{n}(\boldsymbol{\xi}) \\ \ddot{\boldsymbol{q}}_r(\boldsymbol{\xi}) \end{bmatrix} + \begin{bmatrix} \boldsymbol{k}_{sP}^{n} & \\ & \boldsymbol{k}_r \end{bmatrix} \begin{bmatrix} \boldsymbol{q}_{sP}^{n}(\boldsymbol{\xi}) \\ \boldsymbol{q}_r(\boldsymbol{\xi}) \end{bmatrix} + \begin{bmatrix} \boldsymbol{c}_{sP}^{n} & \\ & \boldsymbol{c}_r \end{bmatrix} \begin{bmatrix} \dot{\boldsymbol{q}}_{sP}^{n}(\boldsymbol{\xi}) \\ \dot{\boldsymbol{q}}_r(\boldsymbol{\xi}) \end{bmatrix} = \begin{bmatrix} \boldsymbol{f}_{sP}^{n}(\boldsymbol{\xi}) \\ \boldsymbol{f}_r(\boldsymbol{\xi}) \end{bmatrix}, \tag{23}$$

where there are $n + 2$ degrees of freedom. Due to the nonlinear forces in $\boldsymbol{f}_{sP}^{n}(\boldsymbol{\xi})$ and $\boldsymbol{f}_r(\boldsymbol{\xi})$, it is necessary to convert the response in modal space back to physical space at each step of the numerical calculation. By substituting $\boldsymbol{q}_s(\boldsymbol{\xi}) = \boldsymbol{\Phi}\boldsymbol{q}_{sP}(\boldsymbol{\xi})$, $\dot{\boldsymbol{q}}_s(\boldsymbol{\xi}) = \boldsymbol{\Phi}\dot{\boldsymbol{q}}_{sP}(\boldsymbol{\xi})$ into Equations (1)–(3), the nonlinear forces of $\boldsymbol{f}_1\boldsymbol{f}_2$ and $\boldsymbol{f}_d$ can be derived in physical space. Then $\boldsymbol{f}_s$ and $\boldsymbol{f}_r$ can be obtained by Equations (6) and (7). Transforming $\boldsymbol{f}_s$ into modal space through $\boldsymbol{\Phi}^{\mathrm{T}}\boldsymbol{f}_s(\boldsymbol{\xi})$ and performing an n order truncation, $\boldsymbol{f}_{sP}^{n}(\boldsymbol{\xi})$ can be finally derived.

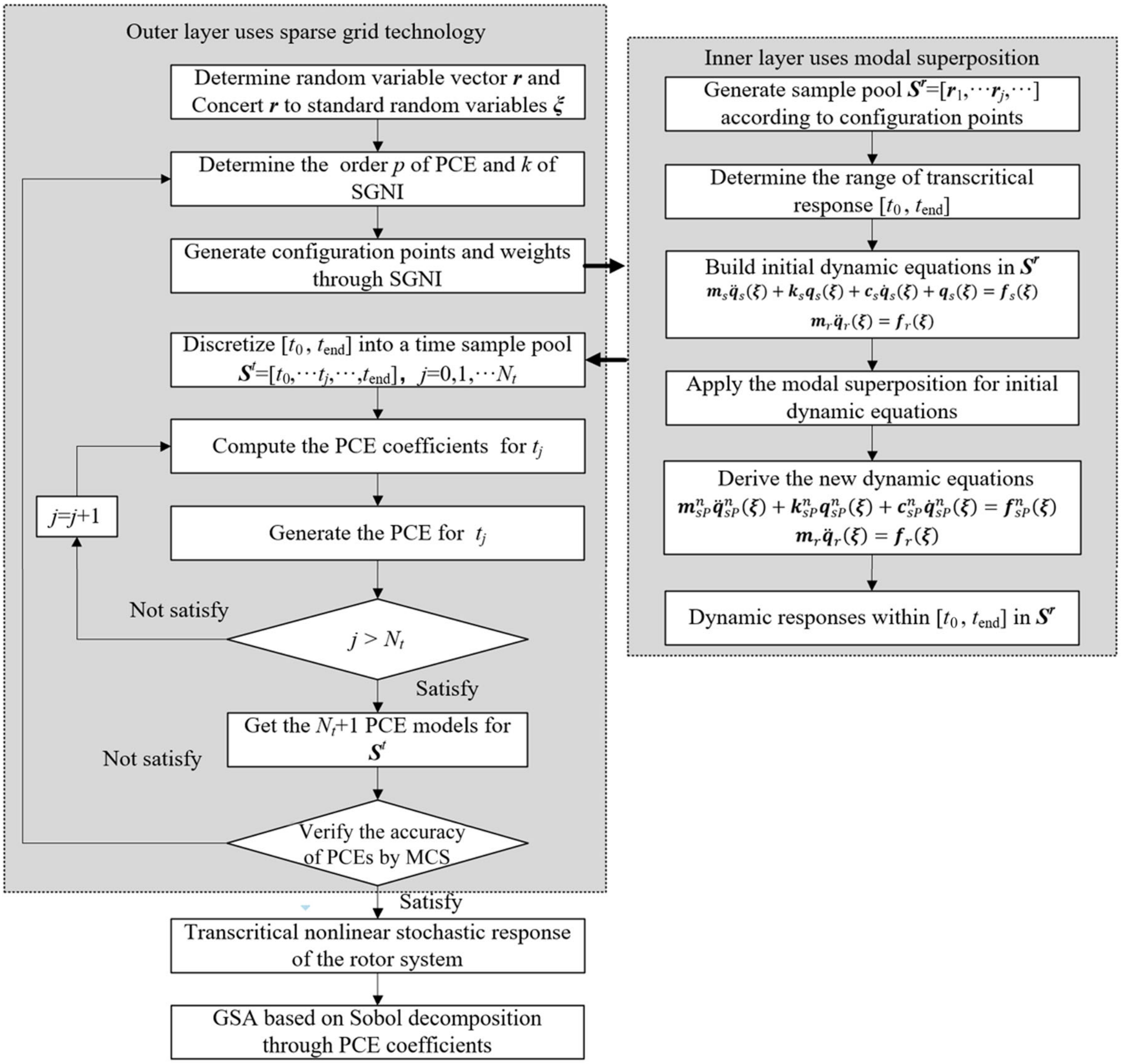

FIGURE 4 | Execution logic for UQ of the supercritical rotor system.

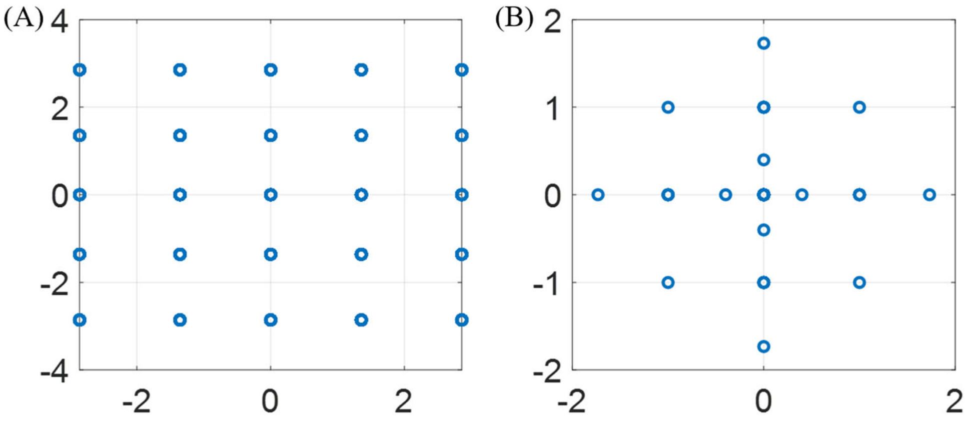

FIGURE 5 | Configuration points through (A) FFNI and (B) SGNI with algebraic accuracy of order 5 for Gauss-Hermite in the two-dimensional standard random space.

TABLE 1 | Values of a helicopter supercritical drive shaft parameters.

Symbol	Description	Value
L	Length	3080 mm
r	Inner radius	56 mm
R	Outer radius	57 mm
ρ	Density	2700 kg/m^3
E	Young's modulus of elasticity	7.1×10^{10} N/m^2
σ	Poisson's ratio	0.3
ζ_1	Damping ratio	0.02
ζ_2	Damping ratio	0.02
ω_1	First natural frequency	215 rad/s
ω_2	Second natural frequency	860 rad/s
e	Eccentricity	0.3 mm
k_0	Stiffness of support	5×10^8 N/m
$\ddot{\phi}$	Acceleration of shaft rotation	20 rad/s^2
ω_o	Operating speed	490 rad/s

TABLE 2 | Deterministic value of the dry friction damper dimensionless parameters.

Symbol	Description	Value
$\bar{m}_r$	Lumped mass	0.07
$\bar{k}_1$	Normal rub-impact stiffness	40
$\bar{k}_2$	Normal rub-impact stiffness	40
μ_1	Tangential rub-impact friction coefficients	0.02
μ_2	Tangential rub-impact friction coefficients	0.02
$\bar{\delta}_1$	Initial clearance	4
$\bar{\delta}_2$	Initial clearance	5
$\bar{f}_c$	Critical dry friction force	3

3.2 | PCE Coefficients Through Sparse Grid Technology

In outer layer, sparse grid technology is applied to get the configuration points, namely sample pool, denoted as $\boldsymbol{S}^r$. To obtain the stochastic transcritical response of the rotorsystem over time, the response derived by solving dynamic equations within the interval $[t_0, t_{\mathrm{end}}]$ is furtherly discretized into a time sample pool $\boldsymbol{S}^t$. In outer layer, PCE models for each time sample point are established. The configuration space of d-dimensional random variables based on SGNI is

$$\Omega_d^n = \bigcup_{k+1\le|\boldsymbol{N}|\le k+d} \Omega_1^{N_1}\otimes\Omega_1^{N_2}\otimes\cdots\Omega_1^{N_j}\otimes\cdots\otimes\Omega_1^{N_d}, \quad (24)$$

where $\boldsymbol{N} = [N_1, N_2, \cdots, N_j, \cdots N_d]$, and $|\boldsymbol{N}| = N_1 + \cdots + N_j + \cdots + N_d$. Using SGNI, the expectation operator can be expressed as

$$E[g] \approx \sum_{i_1=1}^{N_1} w_1^{i_1}\cdots\sum_{i_j=1}^{N_j} w_1^{i_j}\cdots\sum_{i_d=1}^{N_d} w_1^{i_d} g\left(l_1^{i_1},\cdots,l_1^{i_j},\cdots,l_1^{i_d}\right), \quad (25)$$

where $l_1^{i_j}$ and $w_1^{i_j}$, $i_j = 1, 2, \cdots, N_j$ are the i_j-th configuration point and the corresponding quadrature weight of the j-th dimensional variable and $g(l_1^{i_1},\cdots,l_1^{i_j},\cdots,l_1^{i_d})$ is the output response corresponding to configuration point. By substituting $g = q(\boldsymbol{r})\Psi_i(\boldsymbol{\xi})$, and $g = \Psi_i(\boldsymbol{\xi})^2$ into Equation (25), $E[q(\boldsymbol{r})\Psi_i(\boldsymbol{\xi})]$ and $E[\Psi_i(\boldsymbol{\xi})^2]$ can be derived. To calculate $\Psi_i(\boldsymbol{\xi})$, the configuration points for $q(\boldsymbol{r})$ need to be converted to standard random variables. When $\boldsymbol{r}$ follows the normal, uniform, exponential distribution, etc., values of $l_1^{i_j}$ and $w_1^{i_j}$ can be directly derived from the Gauss-Hermite, Gauss-Legendre, and Gauss-Laguerre quadrature formula [39], which can be obtained by consulting a chart. The quadrature weight corresponding to the configuration point $(l_1^{i_1},\cdots,l_1^{i_j},\cdots,l_1^{i_d})$ is

$$w_d^{i_1,i_2,\cdots,i_j,\cdots,i_d} = (-1)^{k+d-|\boldsymbol{N}|}\binom{d-1}{k+d-|\boldsymbol{N}|}\left(w_1^{i_1}w_1^{i_2}\cdots w_1^{i_j}\cdots w_1^{i_d}\right), \quad (26)$$

where k is an integral precision control parameter corresponding to algebraic accuracy of order $2k+1$ [40]. The truncation order p

of PCE and the value of k in SGNI also need to be matched to obtain the accuracy results. Equation (24) means only points that satisfy $k + 1 \leq |\boldsymbol{N}| \leq k + d$ are needed, effectively decreasing the number of configuration points by eliminating certain unimportant quadrature points compared to FFNI, as shown in Figure 5. And the higher the dimension of random variables, the more obvious the advantage of sparse grids.

4 | Results and Discussion

In this section, the effects of uncertainties on the transcritical response of the shaft and dry friction damper system are studied. For each stochastic variable, dispersion is taken around the mean equal to its corresponding deterministic value. The deterministic values of a supercritical drive shaft parameters are shown in Table 1.

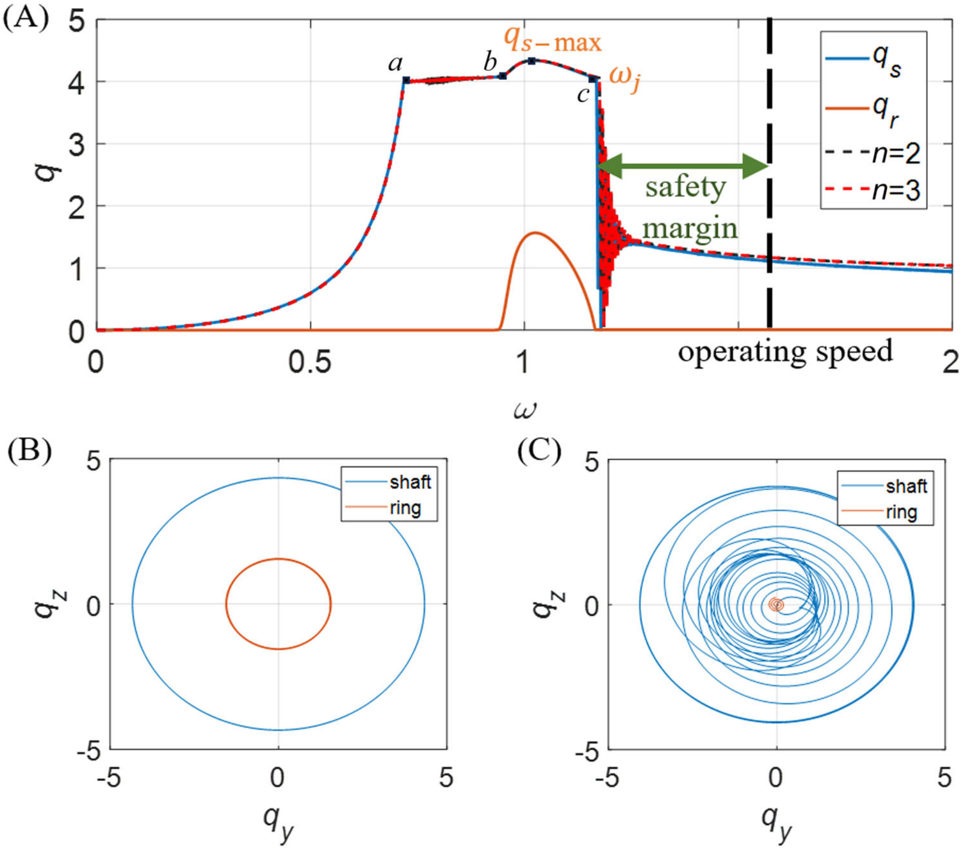

FIGURE 6 | Deterministic transcritical response of the shaft and ring: (A) transient responses of the shaft and ring, (B) orbits of the shaft and ring during b-c phase, and (C) orbit of the shaft and ring during jump phase.

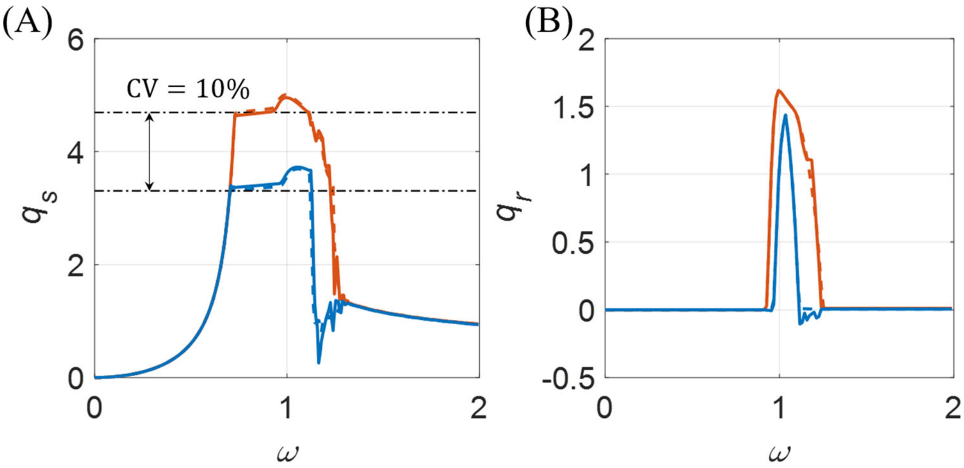

FIGURE 7 | Transcritical response of the system with uncertain δ_1: (A) shaft (B) ring (red = high bound, bule = lower bound, dashed = MCS, and solid = PCE.

Moreover, the parameters of the rotor system are converted into dimensionless form as follows

$$\bar{\boldsymbol{m}}_s = \frac{\boldsymbol{m}_s}{m}, \quad \bar{\boldsymbol{m}}_r = \frac{\boldsymbol{m}_r}{m}, \quad \bar{\boldsymbol{k}}_s = \frac{\boldsymbol{k}_s}{k}, \quad \bar{\boldsymbol{c}}_s = \frac{\boldsymbol{c}_s}{\sqrt{km}},$$

$$\omega = \frac{\dot{\phi}}{\sqrt{k/m}},$$

$$\bar{k}_1 = \frac{k_1}{k}, \quad \bar{k}_2 = \frac{k_2}{k}, \quad \bar{\delta}_1 = \frac{\delta_1}{e}, \quad \bar{\delta}_2 = \frac{\delta_2}{e}, \quad \bar{f}_c = \frac{f_c}{ke}, \tag{27}$$

where $m = 1.43\,\mathrm{kg}$, $k = 66.2\,\mathrm{kN/m}$, are, respectively, the equivalent mass and equivalent stiffness of the shaft can be calculated by treating the drive shaft as a simply supported beam. The other parameters of the rotor system are also non-dimensionalized following the rules specified in Equation (27), which are not presented here for brevity. The deterministic value of the dimensionless parameters of the dry friction damper are set in Table 2.

4.1 | Modal Validation

The deterministic transcritical response of the shaft and the rub-impact ring of damper are derived based on the deterministic parameters shown in Tables 1 and 2. All the transient responses are provided as the deflection of the geometric center of shaft middle node and ring, that is, $q_s = \sqrt{\bar{y}_s^2 + \bar{z}_s^2}$ and $q_r = \sqrt{\bar{y}_r^2 + \bar{z}_r^2}$ and dimensionless. The deterministic transcritical response of the shaft with different truncated orders are shown in Figure 6, where q_s and q_r are derived from the direct numerical calculation of the original equation. It can be seen that a convergent response can be achieved with truncation

TABLE 3 | Statistical properties of input uncertain parameters.

Case	Parameters	Distribution	Mean	Lower limit	Upper limit	CV
1	$\bar{m}_r$	Uniform	0.07	0.0579	0.0821	0.1
2	$\bar{k}_1$	Uniform	40	33.0718	46.9282	0.1
3	μ_1	Uniform	0.02	0.0165	0.0235	0.1
4	$\bar{\delta}_1$	Uniform	4	3.3072	4.6928	0.1
5	$\bar{f}_c$	Uniform	3	2.4804	3.5196	0.1

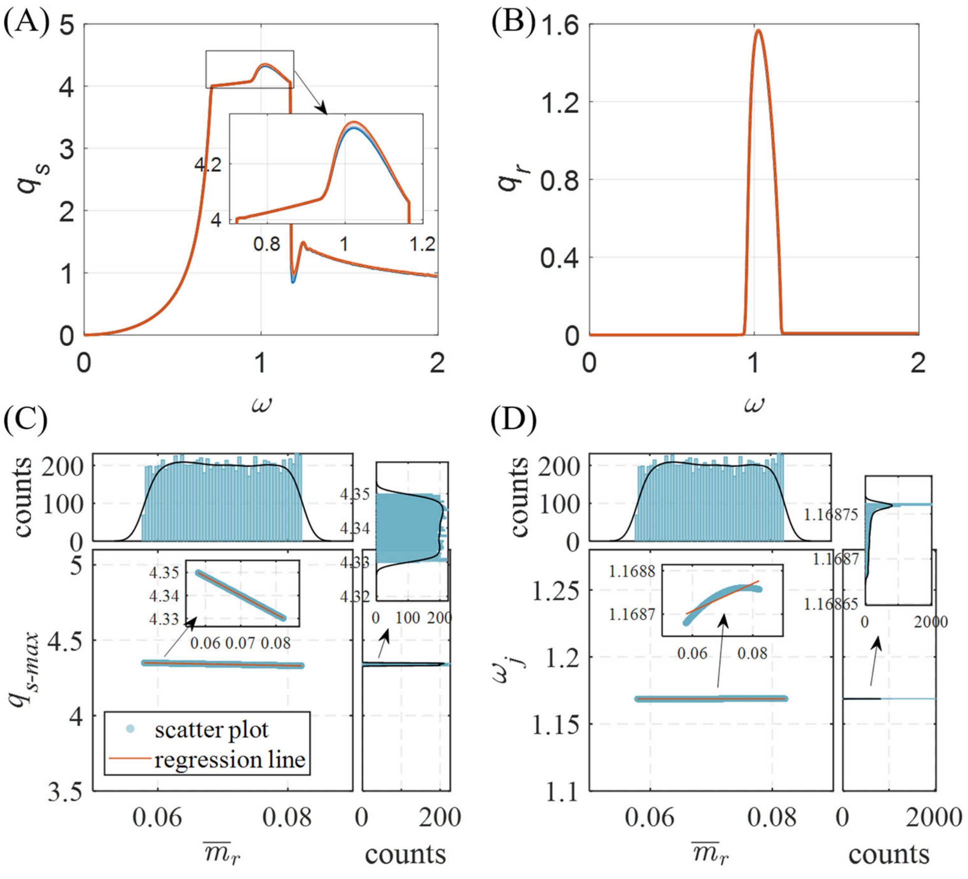

FIGURE 8 | Stochastic transcritical responses of the system for Case 1: (A) shaft, (B) ring, PDFs of (C) $q_{s-\max}$, and (D) ω_j.

order 3. Therefore, $n = 3$ is selected as the final modal truncation order for the calculations that follow.

It can be seen that, with the frequency increases, the vibration of the shaft exceeds $\bar{\delta}_1$ and contact with the rub-impact ring, which keeps sticking under the pre-tightening force during *a-b* phase. When rub-impact force overcomes the critical dry friction force, the ring turns into sliding as shown in *b-c* phase, the orbits of shaft and ring during this phase are shown in Figure 6B. A jump phenomenon occurs at point *c*, resulting in the shaft departing from the ring. The orbit of the shaft, illustrating this departure, is clearly depicted in Figure 6C. During the jump phase, the system is unstable. Phase *a-c* is the called transcritical region of the system and the maximum amplitude of shaft is denoted as $q_{s-\max}$. The frequency of the point *c* called jump frequency is denoted as ω_j, which is an important indicator in determining the safety margin between the operating speed and the critical area as shown in Figure 6A. Therefore, both $q_{s-\max}$ and ω_j are crucial parameters of concern in design.

Considering $\bar{\delta}_1$ follows a uniform distribution with a coefficient of variation of 10%, the PCE is performed to derive the uncertain transcritical response. To verify the accuracy of the PCE, a MCS is performed with 1000 samples. A convergence study of the stochastic response with the order of p and k is performed by comparing with the result from MCS. The upper and lower bounds are derived by percentile difference method [41] with 95% confidence bounds. It has been found that the PCE model with an order $p = 3, k = 5$ which means the calculation of only seven samples, exhibits good consistency with the MCS method, as shown in Figure 7. Therefore, the PCE approach with an order $p = 3, k = 5$ is ultimately employed in this study.

4.2 | Effect of the Uncertain Parameters

In this section, we investigate several cases with different random uncertainties. The stochastic response of the rotor system is obtained considering the uncertainty of five design parameters with coefficients of variation of 10%. The values of the deterministic physical parameters of the rotor are given in Table 2. The random parameters are summarized in Table 3 for each case, where CV means coefficient of variation.

The stochastic response has been verified by MCS for each case, which are not presented here for brevity. The stochastic responses of the shaft and ring are shown in Figures 8–12 for Case 1–Case 5. Furthermore, to illustrate the damping effect of the damper under different parameter uncertainties, the probability distribution functions (PDFs) of $q_{s-\max}$ and ω_j are obtained by establishing the PCE models of $q_{s-\max}$ and ω_j and then performing MCS with 10000 points on these models. Furthermore, the scatterplots with regression lines illustrating the relationships between $q_{s-\max}$ and the parameters, as well as ω_j and the parameters, are presented.

With the uncertainty of $\bar{m}_r$, the shaft's response exhibits slight dispersion in the *b-c* phase, while remaining unaffected in other

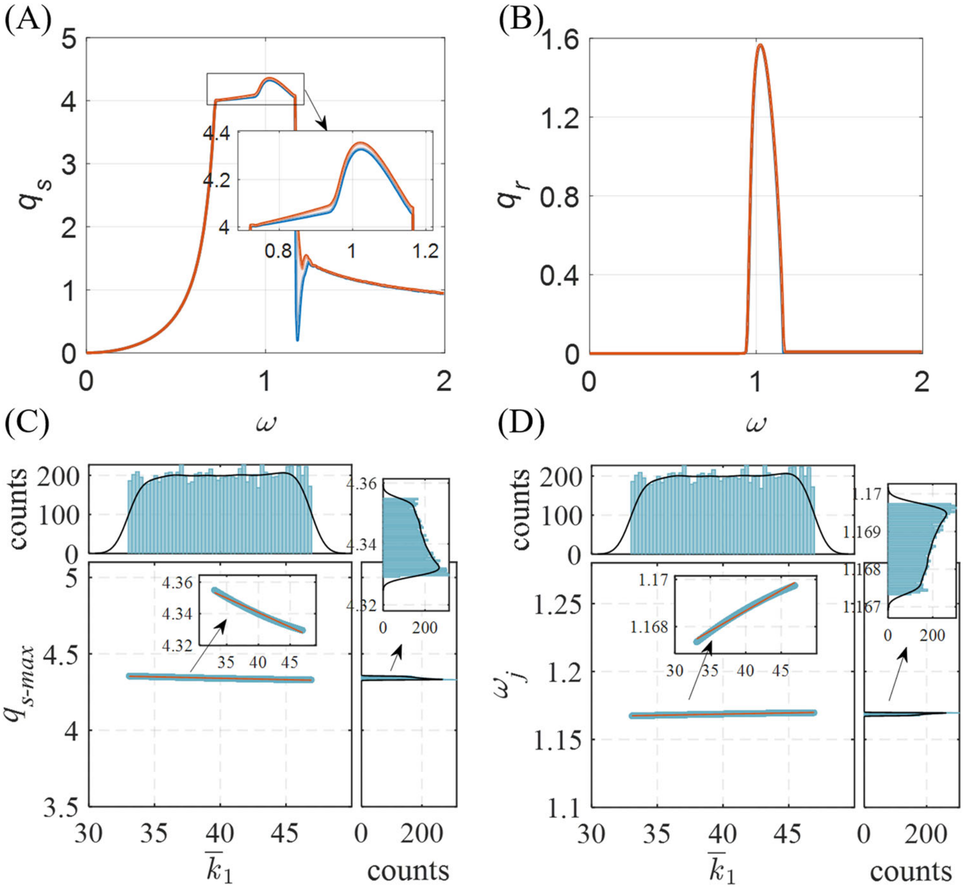

FIGURE 9 | Stochastic transcritical response of the system for Case 2: (A) shaft, (B) ring, PDFs of (C) $q_{s-\max}$, and (D) ω_j.

phases due to the stationary state of the ring, as illustrated in Figure 8A. The response of the ring shows minimal dispersion and remains largely unaffected as shown in Figure 8B. $q_{s-\max}$ exhibits a certain degree of dispersion following with uniform distribution, negatively correlated with $\bar{m}_r$ as shown in Figure 8C. While ω_j exhibits a little degree of dispersion following with right-skewed distribution, positively correlated with $\bar{m}_r$ as shown in Figure 8D. With the uncertainty of $\bar{k}_1$, the shaft's response in the *a-c* phase exhibits a slight degree of dispersion, while the ring's response shows minimal dispersion, as shown in Figure 9A,B. $q_{s-\max}$ and ω_j show a certain degree of dispersion following with left-skewed distribution and right-skewed distribution, respectively. And $q_{s-\max}$ negatively correlates with $\bar{k}_1$ while ω_j positively correlated with $\bar{k}_1$. The entire transcritical process appears to be minimally influenced by μ_1 as shown in Figure 10A,B. This is due to the ring being made of self-lubricating material, resulting in a very low value for μ_1 and ensuring the system remains stable. With the uniform distribution of μ_1, $q_{s-\max}$ and ω_j follow a skewed distribution as shown in Figure 10C,D. The transcritical response of shaft and ring in *a-c* phase are notably affected by the uncertainty of $\bar{\delta}_1$, exhibiting significant deviation as shown in Figure 11A,B. The uncertainty of $\bar{\delta}_1$ led to significant variations in $q_{s-\max}$ and ω_j both distributed uniformly in Figure 11C,D. It can be seen that the correlation between $q_{s-\max}$ and $\bar{\delta}_1$ is very significant, with a negative correlation shown in Figure 11C, while there is a clear positive correlation between ω_j and $\bar{\delta}_1$, as shown in Figure 11D. The uncertainty of $\bar{f}_c$ introduces a degree of dispersion in phase *b-c*, with the point *c* displaying variations, as shown in Figure 12A,B. It can be seen that $q_{s-\max}$ and ω_j show a certain degree of dispersion following with uniform distribution, and $q_{s-\max}$ negatively correlates with $\bar{f}_c$ while ω_j positively correlated with $\bar{f}_c$. From Figures 8–12, it can be seen that the stochastic transcritical response of the system still holds the shape of typical transcritical process. The response far from transcritical region is unaffected by parameter uncertainty, whereas the transcritical region, $q_{s-\max}$ and ω_j exhibit a certain degree of deviation. Additionally, $q_{s-\max}$ and ω_j show an inverse correlation with the uncertain parameters.

4.3 | GSA and Key Parameters Optimization

A Sobol global sensitivity analysis is analytically performed as the post-processing of PCE to obtain the key parameters and combinations thereof of the damper affecting the maximum amplitude and jump frequency. The values of maximum amplitude and jump frequency with the uncertainty of five design parameters shown in Table 3 are derived from the present method with 3002 grids, while 7776 grids are need in FFNI and more than 10 000 samples are needed in MCS. The comparison of the first-order and the total sensitivity indices of $q_{s-\max}$ is presented in Figure 13A. It can be found that the $q_{s-\max}$ is most sensitive to the initial clearance between shaft and ring ($\bar{\delta}_1$) while insensitive to other parameters. And the first-order Sobol indices of each uncertain parameter are close to its total Sobol indices, which means that the interact effects of the five parameters are minor, as shown in Figure 13B. The

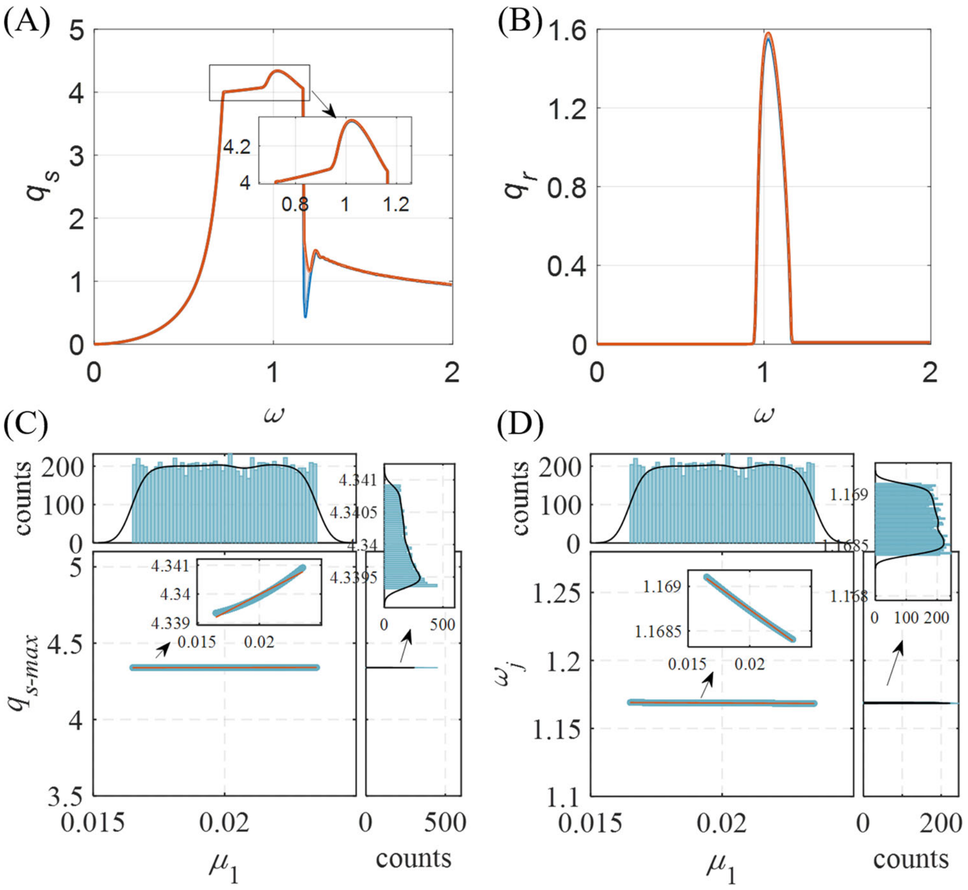

FIGURE 10 | Stochastic transcritical response of the system for Case 3: (A) shaft, (B) ring, PDFs of (C) $q_{s-\max}$, and (D) ω_j.

Sobol sensitivity indices of ω_j are presented in Figure 14A. By comparison, it can be observed that ω_j is much more sensitive to $\bar{\delta}_1$, then followed by $\bar{f}_c$, and insensitive to the other parameters. The interact effects of the parameters are shown in Figure 14B. It can be seen that the interact effects to ω_j are also minor.

In conclusion, $q_{s-\max}$ and ω_j are highly sensitive to variations in $\bar{\delta}_1$ and $\bar{f}_c$, making them crucial design parameters. However, in Figures 11 and 12, inverse correlations can be observed between $\bar{\delta}_1$ and $q_{s-\max}$, $\bar{\delta}_1$ and ω_j, as well as $\bar{f}_c$ and $q_{s-\max}$, $\bar{f}_c$and ω_j. This suggests that it is not feasible to decrease $q_{s-\max}$ and ω_j simultaneously, a trade-off between them is necessary. Therefore, it is crucial to carefully choose the values of $\bar{\delta}_1$ and $\bar{f}_c$ to maintain optimal values for both $q_{s-\max}$ and ω_j.

A key parameters optimization aiming to minimize $q_{s-\max}$ and ω_j is further conducted. $\bar{m}_r$, $\bar{k}_1$ and μ_1 remain unchanged shown in Table 2, further optimization is conducted for $\bar{\delta}_1$ and $\bar{f}_c$ with design ranges of $2 < \bar{\delta}_1 < 8, 1 < \bar{f}_c < 7$, respectively. The PCE is performed to establish a surrogate model with $\bar{\delta}_1$ and $\bar{f}_c$ as inputs and $q_{s-\max}$ as output, as well as a surrogate model with $\bar{\delta}_1$ and $\bar{f}_c$ as inputs and ω_j as output. To do that, assuming that $\bar{\delta}_1$ follows a uniform distribution on the interval $[2, 8]$, and $\bar{f}_c$ follows a uniform distribution on the interval $[1, 7]$, convert them into standard random variables denoted as ξ_1 and ξ_2. For the convenience of expression, the PCE model of $q_{s-\max}$ is written as $y_1 = f_1(\xi_1, \xi_2)$ and the PCE model of ω_j is written as $y_2 = f_2(\xi_1, \xi_2)$. The accuracy of the PCE models has been examined. The mathematical model for the multi-objective optimization of the damper can be written as

$$\left\{\begin{matrix} \min Y = (f_1(\xi_1, \xi_2), f_2(\xi_1, \xi_2)) \\ \text{s.t.} \quad 2 < \bar{\delta}_1 < 8 \\ \quad 1 < \bar{f}_c < 7 \end{matrix}\right\}. \tag{28}$$

In this paper, NSGA-II algorithm [42] is used to solve the optimization problem, which is one of the currently popular multi-objective genetic algorithms with the advantages of fast running speed and good convergence of solution sets. In the integration of PCE models with NSGA-II optimization, the resulting optimization outcome is visually presented in Figure 15A. By analyzing the Pareto front generated, point A is identified as the optimal choice, and point B represents the outcome with the initial set of parameters before optimization. The transcritical response of the shaft with the parameters at point A, that is, $\bar{\delta}_1 = 3.4$, $\bar{f}_c = 1.5$ is shown in Figure 15B. It clearly shows a decrease in both the maximum amplitude and jumping frequency of the shaft compared to initial result. This indicates a notable enhancement in the vibration reduction performance of the dry friction damper. The results signify a successful optimization effort that has effectively reduced vibration levels, leading to improved overall performance.

4.4 | Experimental Verification

To verify the dynamic model and optimization design method, experiments are carried out on a supercritical rotor rig. The experimental device is shown in Figure 16, which consists of a

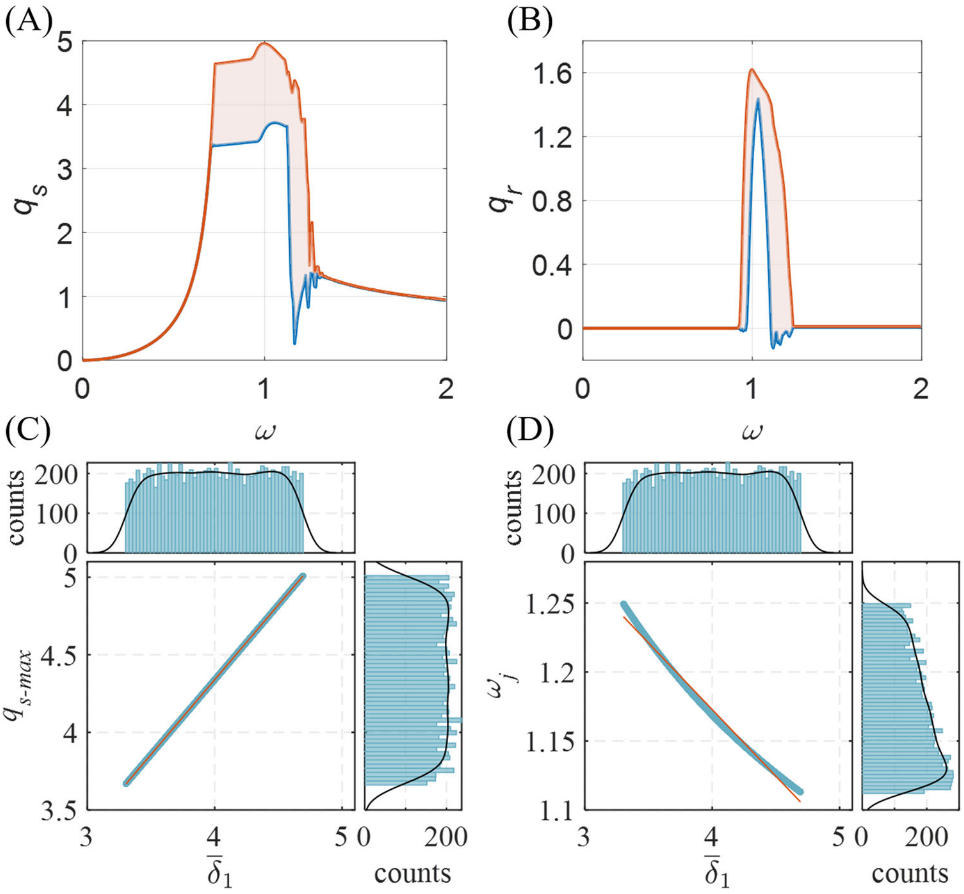

FIGURE 11 | Stochastic transcritical response of the system for Case 4: (A) shaft, (B) ring, PDFs of (C) $q_{s-\max}$, and (D) ω_j.

rotor test bench, a dry friction damper and a signal acquisition system. The dry friction damper is installed on the middle of the long shaft which is a supercritical rotor. To measure the transcritical vibration response of the shaft, the displacement sensors are installed in both horizontal and vertical directions near the dry friction damper. The rotor system is derived by a 380 V three-phase asynchronous motor and the speed can be adjusted continuously from 0 to 4500 r/min. In this experiment, the rotor system is accelerated from 0 to 4000 r/min, making the long shaft cross the critical speed. The transcritical vibration response of the shaft is obtained through displacement sensors and signal acquisition system. The dynamic model of the experimental rotor system is established as shown in Figure 17 based on the modeling method proposed in Section 2. The main simulation parameters of the experimental system are shown in Table 4. To validate the accuracy of the established dynamic model, four sets of inner diameters of rings are utilized to change the initial clearance δ_1, which are 1, 1.5, 2, and 2.5 mm, respectively, as shown in Figure 18A. The critical dry friction force f_c can be changed by adjusting the length of the spring, and measured by using a tension meter as shown in Figure 18B. The transcritical vibration experiments are conducted, with the peak-to-peak values of the shaft vibration as the maximum amplitude. Each experiment is repeated five times.

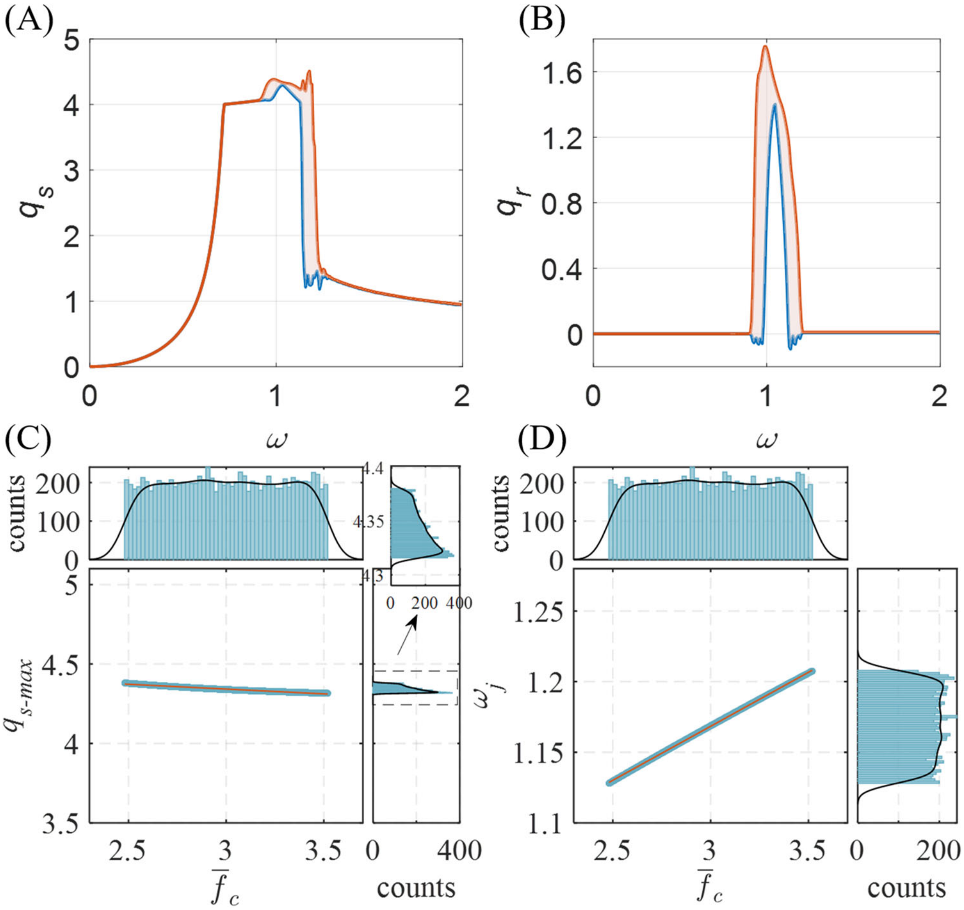

FIGURE 12 | Stochastic transcritical response of the system for Case 5: (A) shaft, (B) ring, PDFs of (C) $q_{s-\max}$, and (D) ω_j.

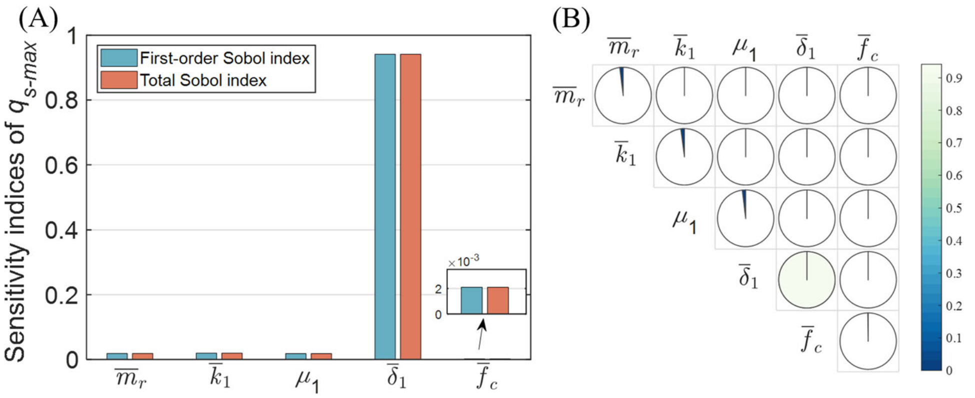

FIGURE 13 | Sobol global sensitivity analysis of $q_{s-\max}$: (A) first-order and total Sobol indices and (B) interact effect of the five parameters.

The comparison of amplitude variation trends under different clearances is depicted in Figure 19, showcasing a maximum error of 1.5% between the simulation results and experimental results, which verify the accuracy of the established dynamic model. Based on the optimization design method proposed above, the parameters of the dry friction damper are optimized, the resulting values of $\delta_1 = 1.5$ mm, $f_c = 10$ N are determined as the optimal parameters for the damper. The comparison of

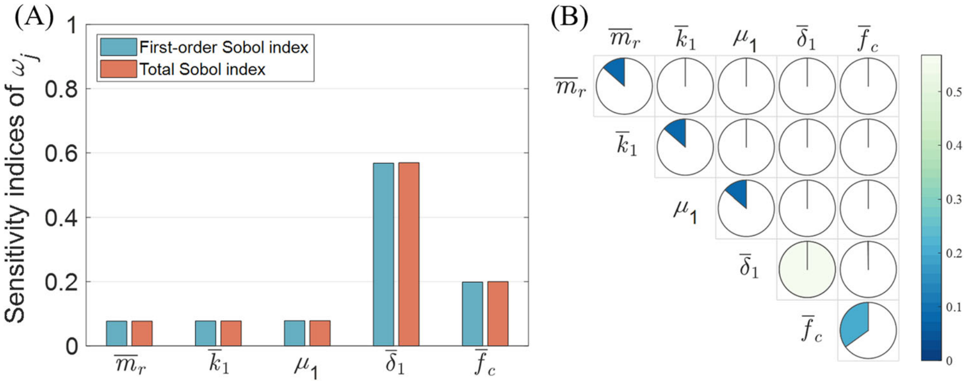

FIGURE 14 | Sobol global sensitivity analysis of ω_j: (A) first-order and total Sobol indices and (B) interact effect of the five parameters.

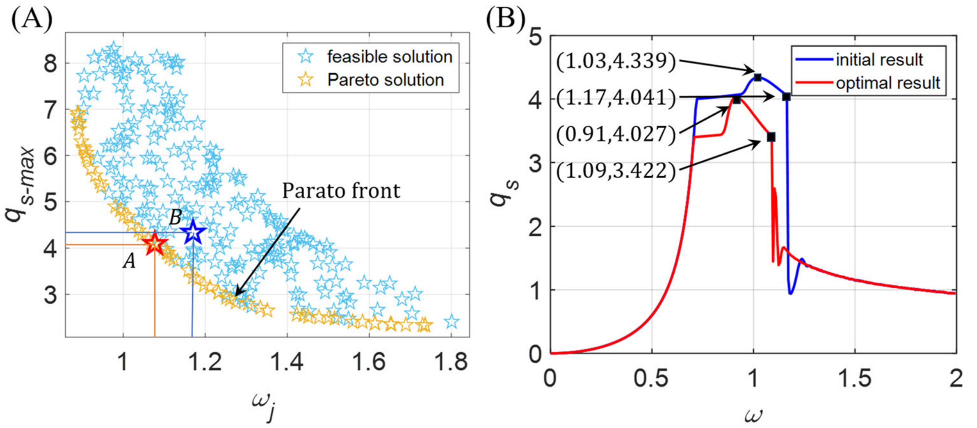

FIGURE 15 | Multi objective optimization results: (A) the optimization outcome based on NSGA-II combined with PCE models (B) the transcritical response of shaft with parameters at point A.

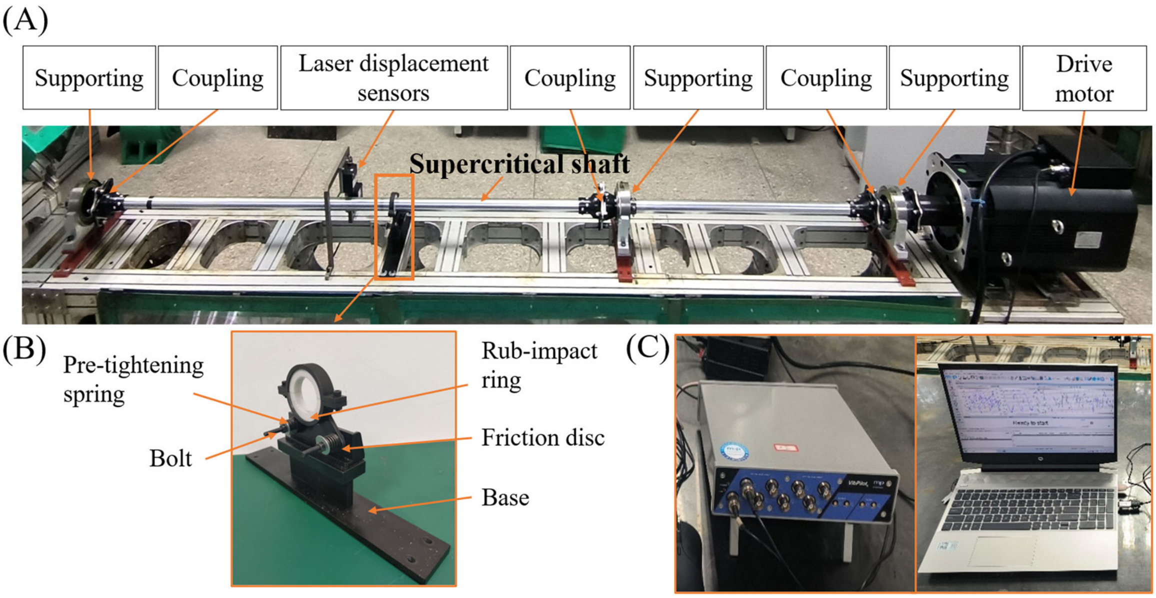

FIGURE 16 | Supercritical rotor experimental rig equipped with a dry friction damper: (A) rotor test bench, (B) dry friction damper, and (C) signal acquisition system.

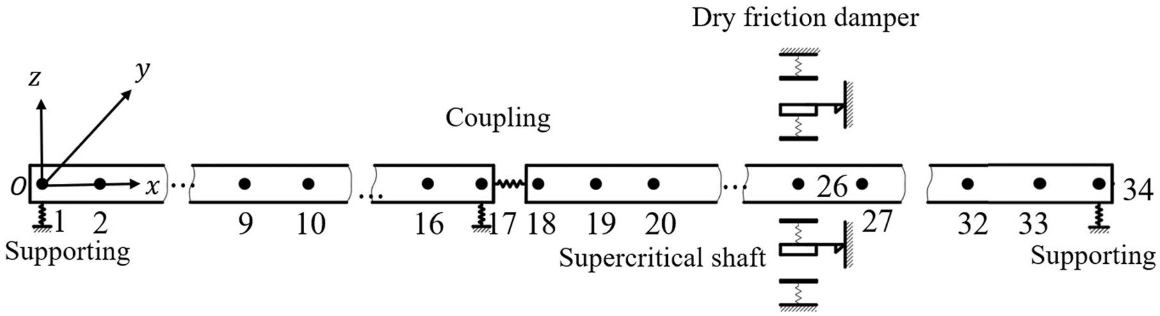

FIGURE 17 | The dynamic model of the experimental rotor system.

TABLE 4 | Value of the main simulation parameters of experimental system.

Symbol	Description	Value
L_1	Length of the short shaft	810 mm
L_2	Length of the long shaft	1635 mm
r	Inner radius	34 mm
R	Outer radius	38 mm
ρ	Density	2700 kg/m^3
E	Young's modulus of elasticity	7.1×10^{10} N/m^2
σ	Poisson's ratio	0.3
e	Eccentricity	0.3 mm
k_0	Stiffness of support	5×10^8 N/m
k_c	Stiffness of coupling	9.9×10^7 N/m
m_r	Lumped mass	0.036 kg
k_1	Normal rub-impact stiffness	9.48×10^5 N/m
k_2	Normal rub-impact stiffness	9.48×10^5 N/m
μ_1	Tangential rub-impact friction coefficients	0.04
μ_2	Tangential rub-impact friction coefficients	0.04
δ_1	Initial clearance	2 mm
δ_2	Initial clearance	2 mm
f_c	Critical dry friction force	30 N

experimental results before and after optimization design is shown in Figure 20. It can be seen that the amplitude of the shaft is reduced, yet still maintaining a small range of transcritical region, indicating the effectiveness of the optimization method.

5 | Conclusions

In this paper, a stochastic dynamic model for the uncertainty and sensitivity analysis of a supercritical rotor system is established, using PCE method and a double-layer dimensionality reduction algorithm. The uncertain dynamic responses of the rotor are derived under different parameter uncertainties and verified by comparison with MCS. The effects of parameter uncertainties are analyzed. A multi-objective optimization design is carried out based on PCE model combined with NSGA-II. The dynamic model of the rotorsystem and the optimization design method are then validated by experiments. The conclusions can be obtained as follows:

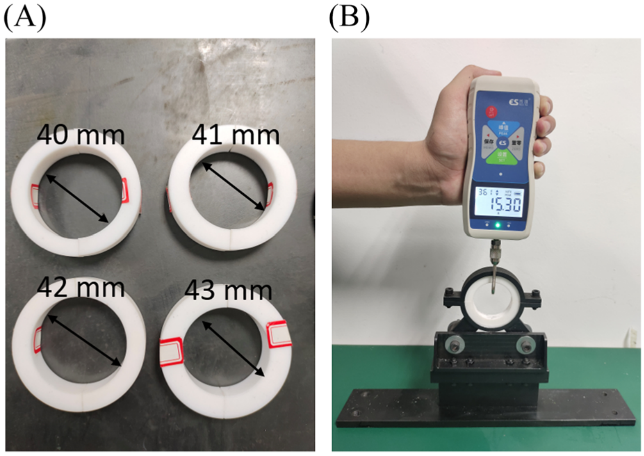

FIGURE 18 | Different parameters of the dry friction damper: (A) rub-impact rings with different inner diameters and (B) the measurement of critical dry friction force f_c.

1. Compared to directly performing MCS on the original dynamic equations, using modal superposition combined with sparse grid techniques can significantly improve the efficiency of uncertainty quantification.
2. With a small variation in design parameters, there exists a certain level of variability in the transcritical response of the rotor, especially the transcritical region.
3. The sensitivity analysis reveals that the transcritical amplitude and jump frequency are highly sensitive to variations in clearance and critical dry friction force. There exist inverse correlations between the two key parameters and damping performance, which suggests that it is not feasible to simultaneously reduce both transcritical amplitude and jump frequency; a trade-off is necessary.
4. The multi-objective optimization design for key parameters demonstrates a clear reduction in both the maximum amplitude and jump frequency of the shaft, indicating a notable improvement in the vibration reduction performance of the dry friction damper.

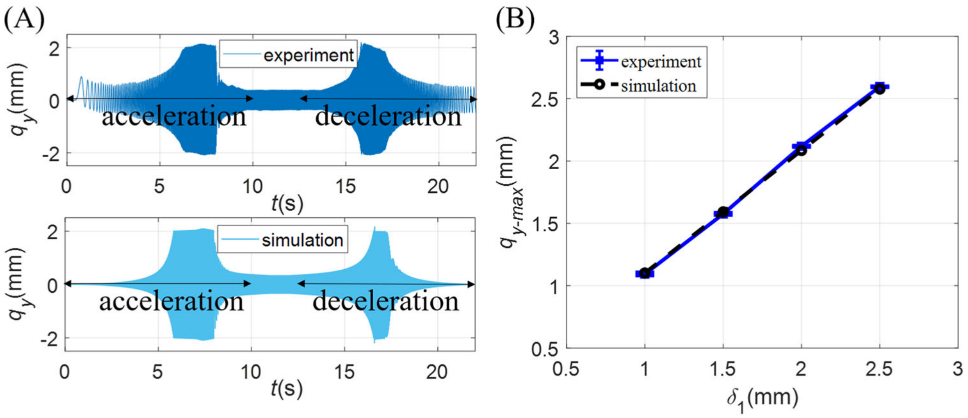

FIGURE 19 | Comparison of simulation and experimental results: (A) transcritical response under parameters in Table 4 and (B) comparison of amplitude variation trends under different clearances.

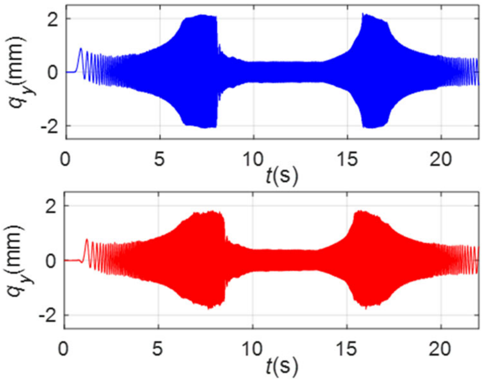

FIGURE 20 | Comparison of experimental results before and after the optimization design.

Acknowledgments

The authors are grateful to the financial supports from Postgraduate Research & Practice Innovation Program of Jiangsu Province (Grant No. KYCX24_0552) and National Natural Science Foundation of China (Grant No. 52005253).

Conflicts of Interest

The authors declare no conflicts of interest.

Data Availability Statement

The data that support the findings of this study are available from the corresponding author, Dan Wang, upon reasonable request.

References

1. P. L. Hetherington, R. F. Kraus, and M. S. Darlow, “Demonstration of a Supercritical Composite Helicopter Power Transmission Shaft,” *Journal of the American Helicopter Society* 35 (1990): 23–28.

2. Q. Mei, “Dynamics Design of Helicopter Drive Shafts,” *Journal of Mechanical Transmission* 29, no. 5 (2005): 19–22.

3. Z. Dżygadło and W. Perkowski, “Nonlinear Dynamic Model for Flexural Vibrations Analysis of a Supercritical Helicopter's Tail Rotor Drive Shaft,” *Prace-Instytut Lotnictwa* 160 (2000): 49–53.

4. Z. Dżygadło and W. Perkowski, “Research on Dynamics of a Supercritical Propulsion Shaft Equipped With a Dry Friction Damper,” *Aircraft Engineering and Aerospace Technology* 74, no. 5 (2002): 447–454.

5. W. Perkowski, “Dry Friction Damper for Supercritical Drive Shaft,” *Journal of KONES. Powertrain and Transport* 23, no. 4 (2016): 389–396.

6. O. Özaydın, *Vibration Reduction of Helicopter Tail Shaft by Using Dry Friction Dampers*. Thesis. Middle East Technical University; 2017.

7. O. Ozaydin and E. Cigeroglu, “Effect of Dry Friction Damping on the Dynamic Response of Helicopter Tail Shaft,” *Rotating Mach. Hybrid Test Methods Vibro-Acoust. Laser Vibrom.* 8 (2017): 23–30.

8. Z. Huang, J. Tan, C. Liu, and X. Lu, “Dynamic Characteristics of a Segmented Supercritical Driveline With Flexible Couplings and Dry Friction Dampers,” *Symmetry* 13, no. 2 (2021): 281.

9. Z. Huang, J. Tan, and X. Lu, “Phase Difference and Stability of a Shaft Mounted a Dry Friction Damper: Effects of Viscous Internal Damping and Gyroscopic Moment,” *Advances in Mechanical Engineering* 13, no. 3 (2021): 1–17.

10. D. Wang, L. Song, R. Zhu, and P. Cao, “Nonlinear Dynamics and Stability Analysis of Dry Friction Damper for Supercritical Transmission Shaft,” *Nonlinear Dynamics* 110 (2022): 3135–3149.

11. D. Wang, L. Song, B. Chen, B. Li, R. Zhu, and H. Wu, “Nonlinear Dynamics of a Supercritical Tail Rotor Drive Shaft Equipped With a Hybrid Damper,” *Journal of Vibration Engineering* 36, no. 3 (2023): 593–605.

12. H. Zhu, S. Hu, L. Zhang, M. Li, and R. Zhu, “Dynamic Characteristics of a Supercritical Helicopter Tail Transmission System With Self-Excited Vibration and Rubbing Impact,” *International Journal of Structural Stability and Dynamics* 24, no. 17 (2024): 1–44.

13. C. Fu, J. J. Sinou, W. Zhu, K. Lu, and Y. Yang, “A State-of-the-Art Review on Uncertainty Analysis of Rotor Systems,” *Mechanical Systems and Signal Processing* 183 (2023): 109619.

14. F. Yamazaki, A. Member, M. Shinozuka, and G. Dasgupta, “Neumann Expansion for Stochastic Finite Element Analysis,” *Journal of Engineering Mechanics* 114, no. 8 (1988): 1335–1354.

15. M. Kamiński, “Generalized Stochastic Perturbation Technique in Engineering Computations,” *Mathematical and Computer Modelling* 51, no. 3–4 (2010): 272–285.

16. A. Guerine, A. El Hami, L. Walha, T. Fakhfakh, and M. Haddar, “A Perturbation Approach for the Dynamic Analysis of One Stage Gear System With Uncertain Nnparameters,” *Mechanism and Machine Theory* 92 (2015): 113–126.

17. E. Denimal and J. J. Sinou, “Advanced Kriging-Based Surrogate Modelling and Sensitivity Analysis for Rotordynamics With Uncertainties,” *European Journal of Mechanics-A/Solids* 90 (2021): 104331.

18. X. Ma, Z. Zhang, and H. Hua, “Uncertainty Quantization and Reliability Analysis for Rotor/Stator Rub-Impact Using Advanced Kriging Surrogate Model,” *Journal of Sound and Vibration* 525 (2022): 116800.

19. F. Xiong, R. Wang, X. Wu, J. Chen, and C. Ren, *Uncertainty Quantification Methods and Applications*, 1st ed. (China Science Publishing & Media Ltd, 2023).

20. L. Wang and G. Yang, *Interval Uncertainty Analysis and Optimization Methods for Engineering Applications*, 1st ed. (China Machine Press, 2022).

21. J. Didier, B. Faverjon, and J. J. Sinou, “Analysing the Dynamic Response of a Rotor System Under Uncertain Parameters by Polynomial Chaos Expansion,” *Journal of Vibration and Control* 18, no. 5 (2012): 712–732.

22. J. Didier, J. J. Sinou, and B. Faverjon, “Study of the Non-Linear Dynamic Response of a Rotor System With Faults and Uncertainties,” *Journal of Sound and Vibration* 331, no. 3 (2012): 671–703.

23. J. Didier, J. J. Sinou, and B. Faverjon, “Multi-Dimensional Harmonic Balance With Uncertainties Applied to Rotor Dynamics,” *Journal of Vibration and Acoustics* 134, no. 6 (2012): 061003.

24. J. Didier, J. J. Sinou, and B. Faverjon, “Nonlinear Vibrations of a Mechanical System With Non-Regular Nonlinearities and Uncertainties,” *Communications in Nonlinear Science and Numerical Simulation* 18, no. 11 (2013): 3250–3270.

25. J. J. Sinou, J. Didier, and B. Faverjon, “Stochastic Non-Linear Response of a Flexible Rotor With Local Non-Linearities,” *International Journal of Non-Linear Mechanics* 74 (2015): 92–99.

26. C. Fu, Y. Xu, Y. Yang, et al., “Response Analysis of An Accelerating Unbalanced Rotating System With Both Random and Interval Variables,” *Journal of Sound and Vibration* 466 (2020): 115047.

27. Z. Jia, Y. Yang, Q. Zheng, and W. Deng, “Dynamic Analysis of Jeffcott Rotor Under Uncertainty Based on Chebyshev Convex Method,” *Mechanical Systems and Signal Processing* 167 (2022): 108603.

28. C. Fu, W. Zhu, Y. Yang, S. Zhao, and K. Lu, “Surrogate Modeling for Dynamic Analysis of an Uncertain Notched Rotor System and Roles of Chebyshev Parameters,” *Journal of Sound and Vibration* 524 (2022): 116755.

29. C. Fu, W. Zhu, Z. Zheng, C. Sun, Y. Yang, and K. Lu, “Nonlinear Responses of a Dual-Rotor System With Rub-Impact Fault Subject to Interval Uncertain Parameters,” *Mechanical Systems and Signal Processing* 170 (2022): 108827.

30. C. Fu, K. Zhang, H. Cheng, et al., “A Comprehensive Study on Natural Characteristics and Dynamic Responses of a Dual-Rotor System With Inter-Shaft Bearing Under Non-Random Uncertainty,” *Journal of Sound and Vibration* 570 (2024): 118091.

31. Z. Zhang, X. Ma, H. Hua, and X. Liang, “Nonlinear Stochastic Dynamics of a Rub-Impact Rotor System With Probabilistic Uncertainties,” *Nonlinear Dynamics* 102 (2020): 2229–2246.

32. X. Ma, Y. Zhong, P. Cao, J. Yuan, and Z. Zhang, “Uncertainty Quantification and Sensitivity Analysis for the Self-Excited Vibration of a Spline-Shafting System,” *ASCE-ASME Journal of Risk and Uncertainty in Engineering Systems, Part B: Mechanical Engineering* 9, no. 4 (2023): 041104.

33. B. Sudret, “Global Sensitivity Analysis Using Polynomial Chaos Expansions,” *Reliability Engineering & System Safety* 93, no. 7 (2008): 964–979.

34. D. Xiu and G. E. Karniadakis, “The Wiener--Askey Polynomial Chaos for Stochastic Differential Equations,” *SIAM Journal on Scientific Computing* 24, no. 2 (2002): 619–644.

35. I. M. Sobol, “Global Sensitivity Indices for Nonlinear Mathematical Models and Their Monte Carlo Estimates,” *Mathematics and Computers in Simulation* 55, no. 1–3 (2001): 271–280.

36. D. H. Evans, “An Application of Numerical Integration Techniques to Statistical Tolerancing, III: General Distributions,” *Technometrics* 14, no. 1 (1972): 23–35.

37. H. J. Bungartz and M. Griebel, “Sparse Grids,” *Acta Numerica* 13 (2004): 147–269.

38. H. Devathi and S. Sarkar, “Propagation of Parametric Uncertainties in a Nonlinear Aeroelastic System Using an Improved Adaptive Sparse Grid Quadrature Routine,” *ASCE-ASME Journal of Risk and Uncertainty in Engineering Systems, Part B: Mechanical Engineering* 4, no. 4 (2018): 041009.

39. M. Abramowitz and I. A. Stegun, *Handbook of Mathematical Functions*, 10th ed. (Dover Publications, 1972).

40. S. Chen, J. Tao, H. Zhu, and X. Zeng, “Sparse Grid Based Stochastic Collocation Method for Analog Building Block Behavioral Modeling Under Process Variations,” *Journal of Fudan University (Natural Science)* 47, no. 1 (2008): 56–64+69.

41. B. Huang and X. Du, “Analytical Robustness Assessment for Robust Design,” *Structural and Multidisciplinary Optimization* 34 (2007): 123–137.

42. K. Deb, S. Agrawal, A. Pratap, and T. Meyarivan, “A Fast Elitist Non-Dominated Sorting Genetic Algorithm for Multi-Objective Optimization: NSGA-II,” Paper presented at: International Conference on Parallel Problem Solving From Nature; September 18–20, 2000; Paris, France.

Appendix A

Expressions for Modeling

$$\varepsilon_1 = ((y_s - y_r)^2 + (z_s - z_r)^2)^{1/2} - \delta_1, \tag{A1}$$

$$\varepsilon_2 = ({y_r}^2 + {z_r}^2)^{1/2} - \delta_2, \tag{A2}$$

where y_s, z_s, y_r, z_r are the displacement of the middle note of shaft and damper respectively.

$$v_1 = (\dot{z}_s - \dot{z}_r)\cos\varphi_1 - (\dot{y}_s - \dot{y}_r)\sin\varphi_1 + \dot{\phi} R, \tag{A3}$$

$$v_2 = \dot{z}_r \cos\varphi_2 + \dot{y}_r \sin\varphi_2, \tag{A4}$$

where R is the outer diameter of the shaft, ϕ is the rotation angular of the shaft. A dot over the displacement represents the derivation with time. φ_1, φ_2 are the angles between the normal rub-impact force and y-axis, and can be derived by

$$\cos\varphi_1 = (y_s - y_r)((y_s - y_r)^2 + (z_s - z_r)^2)^{-1/2}, \tag{A5}$$

$$\sin\varphi_1 = (z_s - z_r)((y_s - y_r)^2 + (z_s - z_r)^2)^{-1/2}, \tag{A6}$$

$$\cos\varphi_2 = -y_r({y_r}^2 + {z_r}^2)^{-1/2}, \tag{A7}$$

$$\sin\varphi_2 = -z_r({y_r}^2 + {z_r}^2)^{-1/2}, \tag{A8}$$

$$v_r = ({\dot{y}_r}^2 + {\dot{z}_r}^2)^{1/2}, \tag{A9}$$

$$\boldsymbol{c}_s = a_1 \boldsymbol{m}_s + a_2 \boldsymbol{k}_s, \tag{A10}$$

where a_1 denotes the mass damping coefficient, given by

$$a_1 = \frac{2\omega_1\omega_2(\zeta_1\omega_2 - \zeta_2\omega_1)}{{\omega_2}^2 - {\omega_1}^2}, \tag{A11}$$

and a_2 denotes the stiffness damping coefficient, given by

$$a_2 = \frac{\zeta_2\omega_1 - \zeta_1\omega_2}{{\omega_2}^2 - {\omega_1}^2}. \tag{A12}$$

ζ_1, ζ_2 denote the damping ratios of the first and second modes, respectively, while ω_1, ω_2 denote the first and second natural frequencies.

Appendix B

Influence of Gyroscopic Effect

To illustrate the impact of the gyroscopic effect, Campbell diagrams are plotted with and without the gyroscopic effect using the parameters provided in Table 1, as shown in Figure B1. This diagram illustrates the variation of the rotor's natural frequencies with rotational speed within the range of 0 to 1500 rad/s. In Figure B1A, it can be observed that the rotor exhibits a pair of closely natural frequencies, which are caused by the gyroscopic effect. The black curve represents forward whirl (FW), while the blue curve denotes backward whirl (BW). The red dashed line indicates where the natural frequency equals the rotational speed. The intersection points of this line with the natural frequency curves represent the critical speeds of the rotor, including the first-order forward and backward whirls, as well as the second-order forward and backward whirls. It can be seen that the Campbell diagram of the rotor, when the gyroscopic effect is ignored in Figure B1B, is similar to the result shown in Figure B1A, indicating that the gyroscopic effect has a minimal impact on the system.

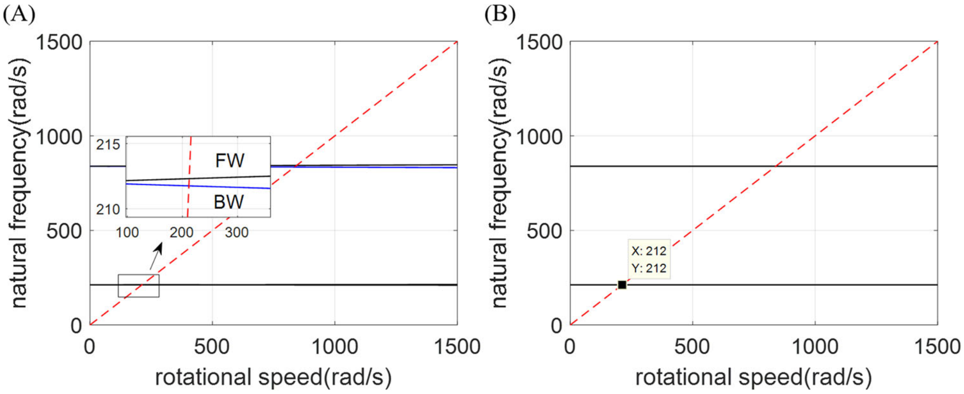

FIGURE B1 | Campbell diagrams of the shaft: (A) considering the gyroscopic effect and (B) ignoring the gyroscopic effect.